Summer 6-24-2024

Sliding Mode Control with Chattering Reduction

Suryamshu Ramesh
Embry-Riddle Aeronautical University, rameshs@my.erau.edu

By

A Thesis Submitted to the Faculty of Embry-Riddle Aeronautical University

In Partial Fulfillment of the Requirements for the Degree of

Master of Science in Aerospace Engineering

Embry-Riddle Aeronautical University

Daytona Beach, Florida

By

THESIS COMMITTEE

Graduate Program Coordinator, Dr. Hever Moncayo	Date
Dean of the College of Engineering, Dr. James W. Gregory	Date
Associate Provost of Academic Support, Dr. Kelly Austin	Date

ACKNOWLEDGMENTS

I would like to thank my advisor, Dr. Dongeun Seo and my advisory committee members Dr. Sergey Drakunov and Dr. Richard Prazenica for introducing Sliding Mode Control to me and their support, knowledge and encouragement. I would like to further thank my family, who have been kind enough to support me financially throughout my education and my friends from India and Anjana Venkat for their gratitude, positivity and constant belief in me to pursue higher education. I could not have pursued this interest of mine without Embry-Riddle Aeronautical University and the professors of the Department of Aerospace Engineering, who have been not only kind but have apprised me of great knowledge during lectures. Lastly, I would like to thank all my peers and friends I have made at this university for their support and good times.

ABSTRACT

Sliding Mode Control is a powerful nonlinear control methodology that can handle parametric uncertainties and external disturbances. However, the discontinuous and high-frequency switching nature of the control law introduces the chattering phenomenon, which leads to potential actuator degradation, alterations to the desired response characteristics and, sometimes, instability during control implementation. The main objective of this thesis is to study Sliding Mode Control with chattering reduction. The Sliding Mode Control law involves an equivalent control component and a discontinuous control component. A disturbance estimation is performed based on Lyapunov analysis and adaptive control techniques and then included in the control law along with the equivalent control term. As a result, the Sliding Mode Control gain can be set to a smaller constant value so as to reduce chattering. The modified controller is tested on a simulation model of the rotational dynamics of a small satellite experiencing constant disturbances using quaternion kinematics and Euler's equations of rotational motion. Furthermore, a Conventional Sliding Mode Controller and an Adaptive Controller are also designed using Lyapunov analysis. The error quaternion and angular velocities are driven towards the identity quaternion and zero respectively using all three control methods and a comparative analysis of the results obtained is conducted.

TABLE OF CONTENTS

LIST OF FIGURES

Figure Page

LIST OF TABLES

NOMENCLATURE

μ	Gravitational Parameter
$\boldsymbol{d}$	Disturbance Torque
$\boldsymbol{q}_e$	Quaternion Error
$\boldsymbol{q}_{\mathcal{B}v}$	Body Quaternion - Vector Component
$\boldsymbol{q}_{\mathcal{B}}$	Body Quaternion
$\boldsymbol{q}_{\mathcal{O}v}$	Orbit Quaternion - Vector Component
$\boldsymbol{q}_{\mathcal{O}}$	Orbit Quaternion
$\boldsymbol{q}_{ev}$	Quaternion Error - Vector Component
$\boldsymbol{s}$	Sliding Manifold Variable
$\boldsymbol{u_{dsc}}$(t)	Sliding Mode Control Discontinuous Control Term
$\boldsymbol{u_{eq}}$(t)	Sliding Mode Control Equivalent Control Term
$\boldsymbol{u_{fb}}$	Feedback Control Term for Adaptive Control Design
$\boldsymbol{u_{inv}}$	Inverse Dynamics Term for Adaptive Control Design
$\boldsymbol{u}$(t)	Control Input
AC	Adaptive Controller
$CSMC$	Conventional Sliding Mode Controller
G	Gain Matrix for Quaternion Error Vector
J	Moment of Inertia Matrix
K	Gain in Adaptive Control Design

SMCD	Sliding Mode Controller with Disturbance Estimation
s	Sliding Surface Variable
U_{max}	Sliding Mode Control - Gain Matrix for Discontinuous Control Term
u_{max}	Sliding Mode Control - Scalar Gain for Discontinuous Control Term
LEO	Low-Earth Orbit
$\mathrm{q}_{\mathcal{B}0}$	Body Quaternion - Scalar Component
$\mathrm{q}_{\mathcal{O}0}$	Orbit Quaternion - Scalar Component
$\mathrm{R}_{\mathcal{BO}}$	Rotation Matrix - from Orbital Frame to Body Frame
SMC	Sliding Mode Control
V	Lyapunov Function
d_o	Disturbance Bound
q_{e0}	Quaternion Error - Scalar Component
${}^{\mathcal{B}}\boldsymbol{h}$	Specific Angular Momentum of the Satellite measured in Body-Frame Components
${}^{\mathcal{B}}\mathbf{R}$	Inertial Position Vector of the Satellite Center of Mass measured in Body-Frame Components
${}^{\mathcal{B}}\mathbf{r}$	Inertial Position Vector of an infinitesimal mass element of the Satellite measured in Body-Frame Components
${}^{\mathcal{B}}\boldsymbol{\omega}$	Body Angular Velocity measured in Body-Frame Components
${}^{\mathcal{B}}\boldsymbol{\omega}_e$	Error Angular Velocity measured in Body-Frame Components

${}^{\mathcal{B}}\boldsymbol{\rho}$	Position Vector of an infinitesimal mass element of the Satellite relative to the Satellite Center of Mass measured in Body-Frame Components
${}^{\mathcal{O}}\boldsymbol{\omega}$	Orbital Angular Velocity measured in Orbit Frame Components

1 Introduction

Sliding Mode Control (SMC) is a nonlinear control scheme notable for its ability to handle bounded parametric uncertainties and external disturbances. SMC is a method that employs multiple control structures to systems using discontinuous switching laws such that the state trajectories are driven towards and constrained to a sliding surface or an intersection of a set of sliding surfaces (also known as a sliding manifold) that is designed based on desired system response characteristics in the state space. Systems of this form are commonly classified under Variable Structure Systems (VSS), and they may inherit properties that neither of the original structures may possess. For example, an asymptotically stable system may consist of two or more structures wherein neither of the structures are stable [1],[2]. SMC consists of a two-part design process: the development of the sliding manifold according to desired response characteristics within the state-space of the system and the deduction of a control law that ensures all the system states converge to the sliding manifold in a finite time interval. In theory, the system states remain on the manifold upon reaching it due to the infinite switching frequency between the multiple control structures and because the sliding manifold is an invariant set, which is termed as ideal sliding mode [3]. The sliding manifold is designed to be of a lower-order than the original system, which allows the system to be studied based on reduced-order dynamics during the sliding phase rather than the full-order dynamics that are typically less robust to parametric variations and external disturbances. Furthermore, the full-order dynamics may be computationally cumbersome in terms of control application and have time response characteristics that may be difficult to quantify (overshoot, damping, etc.) [4]. In real-time application of SMC, ideal sliding mode is not possible because of finite control switching capabilities and imperfections such as parasitic actuator dynamics, unmodeled dynamics, time delays, switching element inertias. Therefore, the system states often experience high-frequency switching in the vicinity of the manifold, causing a phenomenon known as chattering [3]. Chattering is an undesirable characteristic of the real-time application of SMC because it can cause degradation of actuator performance

over time and excite the unmodeled dynamics, which may eventually lead towards undesired system responses and unstable behavior [5].

Several studies have been conducted to develop methods to reduce and eliminate chattering while implementing SMC. One of the most common methods is to select a fixed boundary layer around the vicinity of the sliding manifold, where the discontinuous control term (signum function) can be replaced by a smooth continuous term (saturation function) that is a function of the selected boundary layer width to reduce chattering. However, if the sliding equation is an increasing function and crosses the boundary layer, it is forced back within the boundary due to its attractiveness, which then induces chattering. Also, the selection of a large boundary layer may cause loss of control accuracy [6].

Alternatively, modifications can be made to the conventional discontinuous SMC law such that the constant gain term is replaced by a state-dependent function that can be tuned to decrease as the state trajectories tend towards the manifold, thereby reducing the chattering magnitude. It was also found that the constant gain term could be replaced by a function of the equivalent-control, which is a solution to the first derivative of the sliding surface with respect to the control variable, excluding the external disturbances. The magnitude of the equivalent-control decreases as the states converge to the sliding manifold and, as a result, the chattering magnitude is reduced. However, it was found that real-time implementation of state-dependent and equivalent-control dependent gain methods to reduce chattering was not feasible to systems controlled by fixed switching gains. To address this impracticality, a high-gain observer was employed instead to generate chattering-free sliding mode control in an additional control loop that excludes the plant and unmodeled dynamics. The controller uses estimated states, which are not affected by the unmodeled dynamics and sensor noise. There is a loss of robustness since accurate knowledge of the plant parameters is required to calculate the observer gains. The control design becomes complex due to the inclusion of additional loops, although disturbances, uncertainties and states can be estimated [7].

The methods mentioned above are employed through the modification of the conventional

SMC gain and replacing the discontinuous law with continuous alternatives in a boundary layer around the sliding manifold. With more development in SMC theory since its advent in the 1960s, Terminal Sliding Mode Control (TSMC) was studied to achieve chattering suppression using a nonlinear sliding manifold, which not only provided a faster convergence rate towards the manifold, but increased robustness as noted in [8, 9]. However, the chattering problem still persisted along with issues of complexity in implementation for a wide range of dynamical systems due to singularities in the control law as a result of fractional power functions in the sliding manifold design. Modifications to TSMC have also been of keen interest, such as Nonsingular Terminal Sliding Mode, in which the key development was to ensure the sliding manifold design and control law are singularity-free, therefore providing smoother control action than TSMC [10]; however, most TSMC methods are available only for second-order systems.

Another variation that was studied is Integral Terminal Sliding Mode, wherein an integral term is included in the design of the sliding manifold to eliminate the reaching phase such that chattering is reduced [11]. Higher-Order Sliding Mode Control (HOSMC) and some applications were studied in [12–14], and is based on the selection of sliding manifolds that are higher-order derivatives of the states to ensure finite-time convergence to the manifold in the presence of disturbances and parametric uncertainties. HOSMC eliminates the chattering effectively; however, some design challenges include the unavailability of measurements of all the states, sensitivity to measurement noise and mathematical and computational complexity during real-time implementation. Current developments include the use of neural networks, fuzzy logic and adaptive SMC to handle the chattering problem and highly nonlinear systems, making these techniques popular in academia and research [15–17].

This thesis aims to study Sliding Mode Control with chattering reduction without modification of the conventional SMC structure, the use of nonlinear sliding manifolds, HOSMC, neural networks and adaptive SMC. Chattering reduction, in this study, is rather based on a disturbance parameter estimation via adaptive control, derived using Lyapunov analysis.

The disturbance estimation is included within the continuous equivalent control term of the conventional Sliding Mode Controller, which then allows the reduction of the sliding mode gain to a smaller constant value in the discontinuous control component that contains the *signum* function so as to reduce chattering. The specific application considered is a small satellite attitude control problem, wherein the satellite needs to maintain an Earth-pointing capability while experiencing a constant disturbance in a Low-Earth Orbit (LEO). The reference model is based on the dynamics and kinematics of the orbit described by Euler's equations of motion and quaternion kinematics using the orbit's angular velocity. It is considered that the orbital frame's x-axis points radially outwards along the plane of the orbit. The body-axes of the satellite are chosen such that there is an offset with the orbital frame axes. The control goal is to ensure that the body-axes of the satellite align with the orbital frame's axes and the satellite's and orbit angular velocity vectors are equivalent. In this manner, a camera can be placed along the negative x-axis of the satellite body and Earth-pointing capability can be achieved during the time of flight. Three control methodologies are considered to achieve this control objective: Conventional Sliding Mode Control, Adaptive Control and Sliding Mode Control with Disturbance Estimation. Lyapunov based methods are used to prove the stability of the control design and the disturbance estimation. The results obtained using the proposed control methodology are compared to those obtained using the Conventional Sliding Mode Controller and the Adaptive Controller to highlight chattering reduction and performance differences.

The attitude control of a rigid spacecraft is used to test this control design since it is an extensively studied nonlinear control problem and plays an integral role in the context of space missions. Applications of satellite attitude control extend to formation flight, docking and rendezvous, station-keeping, planned maneuvers, Earth observation and communication. Furthermore, Nanosatellites, CubeSats and other small satellites are subject to various disturbances during space missions as a result of uncertainties in modeling parameters, perturbations due to variations in gravitational and magnetic fields, solar radiation pressure,

atmospheric drag, gravitational forces due to nearby spacecraft and damage due to space debris [18]. Some disturbances can be estimated using existing literature and complex algorithms; nevertheless, model parameter uncertainties and external disturbances always persist during space missions and need to be accounted for in the control law to ensure a spacecraft system provides the desired response [19]. Due to the coupled, nonlinear and multiple-input-multiple-output (MIMO) characteristics of spacecraft kinematics and kinetics, various control methodologies such as adaptive control [20],[21], model predictive control (MPC) [22], back-stepping [23], and feedback linearization [24] have been studied in the past. With recent advancements in technology and increasing popularity of small satellite missions, sliding mode control (SMC) and its several variations offer an advantageous approach to the attitude control problem due to their robustness to bounded model parameter uncertainties and external disturbances [25].

This thesis is structured as follows: Section 2 will provide information regarding the notation used in this thesis and details regarding coordinate transformations, quaternions, and SMC. Section 3 will discuss the development of the satellite kinematics and kinetics using the error quaternion and Euler's equations of motion. Lyapunov analysis will be discussed in Section 4 to show the stability of the control law design and the disturbance estimation. Section 5 will provide details regarding the simulation development and implementation. Simulation results will be discussed in Section 6, and comparisons will be made to results obtained using conventional SMC and the adaptive controller, which then leads to the closing remarks in Section 7.

2 Preliminary Notes

This section will briefly discuss the notation used in this paper to represent matrices, coordinate transformations, vectors and quaternions and their mathematical operations. It will further introduce the fundamentals of SMC and serve as a foundation for the contents discussed later in this thesis.

2.1 Matrices and Vectors

Matrices will be defined by capitalized italic letters; for example, $A \in \mathbb{R}^{n\times n}$, $B \in \mathbb{R}^{m\times n}$. The identity matrix will be represented by I_n, where n is its dimension. Vectors will be denoted by lowercase bold letters, for example $\boldsymbol{a}$, their two-norm will be shown as $\|\boldsymbol{a}\|_2$ and their one-norm will be denoted as $\|\boldsymbol{a}\|_1$. For any two vectors $\boldsymbol{a}$, $\boldsymbol{b} \in \mathbb{R}^3$, the skew-symmetric matrix function $S(\boldsymbol{a})$ can be used to describe the cross-product $\boldsymbol{a} \times \boldsymbol{b} = \boldsymbol{a}^{\times}\boldsymbol{b}$, where $\boldsymbol{a}^{\times}$ and $S(\boldsymbol{a})$ are equivalent and given by:

$$\boldsymbol{a}^{\times} = S(\boldsymbol{a}) = \begin{bmatrix} 0 & -a_3 & a_2 \\ a_3 & 0 & -a_1 \\ -a_2 & a_1 & 0 \end{bmatrix} \tag{2.1}$$

2.2 Coordinate Frames and Transformations

Coordinate transformations can be used to measure the difference between a desired frame of reference and the body-fixed frame of a dynamical system. Vectors can be represented in different frames using coordinate transformations in the form of rotation matrices, also known as attitude matrices. Several frames of reference are utilized for aerospace engineering related applications such as the Earth-Centered Inertial Frame (ECIF), Local Vertical Local Horizontal (LVLH) Frame, perifocal frame, body-fixed frame, etc. Therefore, to maintain notational consistency throughout this thesis, the letter $\mathcal{B}$ will be used to represent the

satellite body-fixed frame, the letter $\mathcal{O}$ will be used to represent the orbital reference frame and the letter $\mathcal{N}$ will be used to represent the inertial frame.

Vectors measured relative to these frames will be denoted by ${}^{B}\boldsymbol{x}$, ${}^{O}\boldsymbol{x}$ and ${}^{N}\boldsymbol{x}$ respectively. Rotation matrices will be represented by the letter R, $R_{\mathcal{BN}}$ is the transformation that maps vectors from the inertial frame into the body-fixed frame and $R_{\mathcal{BO}}$ is the rotation matrix that maps vectors from the orbital reference frame to the body-fixed frame. In general, R_{XY} can be considered as the rotation matrix that transforms vectors in coordinate frame Y to coordinate frame X. Rotation matrices can be in the form of sequential Euler angle rotations, direction cosine matrices (DCM), or quaternions. Euler angles are prone to singularities and nonlinearities in the kinematics, and therefore may not be suitable for attitude description of spacecraft for large angle maneuvers. DCM are singularity-free, but the kinematics require the knowledge of nine parameters with six constraints that need to be accounted for during computation. Quaternions can be made singularity free and their kinematics require the integration of four parameters with a single constraint, which is more numerically stable. Moreover, sequential rotations expressed in terms of DCM and Euler angles require more matrix multiplication, which is more computationally cumbersome than quaternion multiplication. Therefore, considering these advantages, the kinematics and rotation matrices in this paper will be analyzed based on quaternions, which will be described briefly in the next subsection.

2.3 Quaternions

Euler's rotation theorem states that a rigid body can be brought between an initial and final orientation by a single finite rotation (ϕ) about an eigen-axis ($\hat{\boldsymbol{\ell}}$) fixed in the coordinate frames of the initial and final orientation [26]. Using this notion, unit quaternions provide a convenient methodology to describe the attitude of a rigid body in three dimensional space. Quaternions are defined as $\boldsymbol{q} = \begin{bmatrix} q_0 & \boldsymbol{q}_v \end{bmatrix}^T \in \mathbb{R} \times \mathbb{R}^3$ and are comprised of four components, three of which serve as the vector part $\boldsymbol{q}_v = \begin{bmatrix} q_1 & q_2 & q_3 \end{bmatrix} \in \mathbb{R}^3$ and one scalar component

$q_0 \in \mathbb{R}$, satisfying the following holonomic constraint $q_1^2 + q_2^2 + q_3^2 + q_0^2 = 1$ and the following relations:

$$
\begin{aligned}
q_0 &= \cos\frac{\phi}{2} \\
q_1 &= \ell_1 \sin\frac{\phi}{2} \\
q_2 &= \ell_2 \sin\frac{\phi}{2} \\
q_3 &= \ell_3 \sin\frac{\phi}{2}
\end{aligned}
$$

where, $\hat{\boldsymbol{\ell}} = \begin{bmatrix} \ell_1 & \ell_2 & \ell_3 \end{bmatrix}^T$ is the aforementioned eigen-axis about which the rotation takes place. Quaternion addition and subtraction are performed similar to that in vector algebra; however, they are not used for attitude descriptions or in this thesis. Quaternion multiplication provides an efficient way to represent sequential rotations in three-dimensional space. For instance, consider the quaternions $\boldsymbol{r} = \begin{bmatrix} r_0 & \boldsymbol{r}_v \end{bmatrix}^T$, $\boldsymbol{q} = \begin{bmatrix} q_0 & \boldsymbol{q}_v \end{bmatrix}^T$, which both represent a rotation in three-dimensional space. The result of their multiplication can be considered as the sequential rotation first by $\boldsymbol{q}$ and then $\boldsymbol{r}$ combined to a single quaternion $\boldsymbol{p} = \begin{bmatrix} p_0 & \boldsymbol{p}_v \end{bmatrix}^T$ that represents a finite rotation about an eigen-axis. The expansion of this multiplication is provided below and will be useful in the following sections of this thesis.

$$
\boldsymbol{p} = \boldsymbol{r} \otimes \boldsymbol{q} = \begin{bmatrix} r_0 p_0 - \boldsymbol{r}_v^T \boldsymbol{q}_v \\ r_0 \boldsymbol{q}_v + q_0 \boldsymbol{r}_v + \boldsymbol{r}_v^{\times} \boldsymbol{q}_v \end{bmatrix} \tag{2.2}
$$

2.4 Brief Introduction to Sliding Mode Control

As stated previously, the main aim of SMC is to drive the system states to a sliding manifold that is defined based on desired response characteristics of the system in question. When the states reach the manifold, they are expected to handle disturbances and uncertainties. To explain this further, consider a general nonlinear system given by:

$$\dot{\boldsymbol{x}} = f(\boldsymbol{x}, t) + b(\boldsymbol{x})\boldsymbol{u}(t) \tag{2.3}$$

where $\boldsymbol{x} \in \mathbb{R}^n$ is the state vector and $\boldsymbol{u(t)} \in \mathbb{R}^m$ is the control input. The functions $f(\boldsymbol{x})$, $b(\boldsymbol{x})$ may not be known but they can be upper bounded by known continuous functions of $\boldsymbol{x}(t)$ to limit the extent of model uncertainty. Consider the control problem to be such that $\boldsymbol{x}(t)$ needs to track a desired state $\boldsymbol{x_d}(t)$. The tracking error can be defined by $\boldsymbol{e}(t) = \boldsymbol{x}(t) - \boldsymbol{x_d}(t) = \begin{bmatrix} e & \dot{e} & \ddot{e} & ... & e^{n-1} \end{bmatrix}^T$. A sliding equation can then be defined generally in the state-space $\in \mathbb{R}^n$ by:

$$s(\boldsymbol{x}, t) = (\frac{d}{dt} + \lambda)^{(n-1)} e \tag{2.4}$$

where s is scalar, since a single state is driven to zero, and λ is a positive constant. The tracking problem, $\boldsymbol{e} = 0$, now involves making $s(\boldsymbol{x}, t) = 0 \; \forall \; t > 0$ and therefore becomes a measure of the tracking performance. When the equation defined by $s(\boldsymbol{x}, t)$ reaches zero, it is referred to as the sliding manifold. It can be noted that $s(\boldsymbol{x}, t)$ needs to be differentiated once such that the control input $\boldsymbol{u}(t)$ appears in the sliding equation. The control law can then be designed such that the system states are driven to the manifold. However, it must be ensured that once they reach the manifold, they must remain there. Therefore, a reaching condition is enforced, which is given by:

$$\lim_{s \to \; 0^+} \dot{s}(\boldsymbol{x}, t)) < 0 \text{ and } \lim_{s \to \; 0^-} \dot{s}(\boldsymbol{x}, t)) > 0 \tag{2.5}$$

The sliding condition states that the state trajectories must always move towards the sliding manifold, even in the presence of disturbances and uncertainties. There are two phases that the states take before they can undergo sliding mode - the reaching phase and the sliding phase. The reaching phase involves the states converging towards the sliding manifold in finite time, whereas the sliding phase involves landing on the manifold and remaining on it. Both these phases are achieved by involving the following condition in the control design

process:

$$\frac{1}{2}\frac{d(s(\boldsymbol{x},t)^2)}{dt} \leq -\eta s(\boldsymbol{x},t) \tag{2.6}$$

where $\eta > 0$, ensuring that the left-hand side Lyapunov function is less than or equal to zero, implying a stable equilibrium condition.

2.4.1 Equivalent and Discontinuous Control

Given the conditions described in the previous section, the control law is generally considered to be a combination of a continuous and discontinuous control:

$$\boldsymbol{u}(t) = \boldsymbol{u_{eq}}(t) + \boldsymbol{u_{dsc}}(t) \tag{2.7}$$

where $\boldsymbol{u_{eq}}(t)$ is continuous and ensures the sliding mode occurs and $\boldsymbol{u_{dsc}}(t)$ is the discontinuous control responsible for the reaching phase and also compensating for any disturbances and uncertainties during the phase. The $\boldsymbol{u_{eq}}(t)$ is a replacement of the discontinuous control in a boundary around the manifold that ensures the system state velocity vectors are tangential to the sliding manifold [27]. It is derived based on the sliding condition given by $\dot{s}(\boldsymbol{x},t) = 0$, which implies that once the states reach the sliding manifold, they remain there and exhibit desired response characteristics. Therefore, it can be noted that:

$$\dot{s}(\boldsymbol{x},t) = \frac{\partial s(\boldsymbol{x},t)}{\partial \boldsymbol{x}(t)} f(\boldsymbol{x},t) + \frac{\partial s(\mathbf{x},t)}{\partial \boldsymbol{x}(t)} b(\boldsymbol{x})\boldsymbol{u}(t) = 0 \tag{2.8}$$

Assuming $-\left[\frac{\partial s(\boldsymbol{x},t)}{\partial \boldsymbol{x}(t)} b(\boldsymbol{x})\right]^{-1}$ is invertible, the equivalent control term can be expressed by isolating $\boldsymbol{u}(t)$ from Equation 2.8 as:

$$\boldsymbol{u_{eq}}(t) = -\left[\frac{\partial s(\boldsymbol{x},t)}{\partial \boldsymbol{x}(t)} b(\boldsymbol{x})\right]^{-1} \frac{\partial s(\boldsymbol{x},t)}{\partial \boldsymbol{x}(t)} f(\boldsymbol{x},t) \tag{2.9}$$

The discontinuous control term, $\boldsymbol{u_{dsc}}(t)$ is expressed as:

$$\boldsymbol{u_{dsc}}(t) = -u_{max}\,\mathrm{sgn}(s(\boldsymbol{x}, t)) \tag{2.10}$$

where, u_{max} is a constant control gain term. The discontinuous control term ensures finite time convergence to the sliding manifold. It offers robustness to parametric uncertainties and external disturbances. However, it is also responsible for the chattering phenomenon due to the discontinuous nature of the $\mathrm{sgn}(s(\boldsymbol{x}, t))$ function. The magnitude of the u_{max} term determines the level of chattering produced when the sliding mode is enforced.

3 Mathematical Modeling

The rigid satellite kinematics and kinetics will be modeled using quaternions and Euler's equations of rotational motion. The following subsections will discuss the assumptions made in this study, and the details of the satellite and orbit attitude description based on concepts explained in [28, 29].

3.1 Assumptions

To simplify the mathematical model and control design, the following assumptions were made:

- The satellite is rigid, asymmetric and has a uniform and continuous mass distribution
- The satellite's body-fixed axes are centered at its center of mass (c.m) and the principal axes of inertia are aligned with the body-fixed axes
- The moments of inertia of the satellite do not change with time
- The satellite is small in size; hence, the moments of inertia about the principal axes are also small
- The Earth is a rigid sphere with a continuous mass distribution
- The distance between the c.m of the satellite and the c.m of the Earth is much larger than the distance between the c.m of the satellite and any infinitesimal mass point dm on the satellite, as seen in Figure 3.2
- The satellite is subject to a constant disturbance in Low-Earth orbit (LEO)
- The angular velocity and quaternion errors are available via sensor measurements

3.2 Kinematics

The quaternion kinematic differential equation is given by the following expressions:

$$\begin{bmatrix} \dot{q}_{\mathcal{B}0} \\ \dot{\boldsymbol{q}}_{\mathcal{B}v} \end{bmatrix} = \begin{bmatrix} -\frac{1}{2}\boldsymbol{q}_{\mathcal{B}v}^{T}\,{}^{\mathcal{B}}\boldsymbol{\omega} \\ \frac{1}{2}(q_{\mathcal{B}0}I_3 + \boldsymbol{q}_{\mathcal{B}v}^{\times})^{\mathcal{B}}\boldsymbol{\omega} \end{bmatrix} \tag{3.1}$$

$$\begin{bmatrix} \dot{q}_{\mathcal{O}0} \\ \dot{\boldsymbol{q}}_{\mathcal{O}v} \end{bmatrix} = \begin{bmatrix} -\frac{1}{2}\boldsymbol{q}_{\mathcal{O}v}^{T}\,{}^{\mathcal{O}}\boldsymbol{\omega} \\ \frac{1}{2}(q_{\mathcal{O}0}I_3 + \boldsymbol{q}_{\mathcal{O}v}^{\times})^{\mathcal{O}}\boldsymbol{\omega} \end{bmatrix} \tag{3.2}$$

where $\boldsymbol{q}_{\mathcal{B}} = \begin{bmatrix} q_{\mathcal{B}0} & \boldsymbol{q}_{\mathcal{B}v} \end{bmatrix}^T$ refers to the current attitude of the satellite relative to the inertial frame and $\boldsymbol{q}_{\mathcal{O}} = \begin{bmatrix} q_{\mathcal{O}0} & \boldsymbol{q}_{\mathcal{O}v} \end{bmatrix}^T$ is the orbital frame attitude relative to the inertial frame. $\boldsymbol{q}_{\mathcal{B}}$ and $\boldsymbol{q}_{\mathcal{O}} \in \mathbb{R} \times \mathbb{R}^3$. In Equations 3.1 and 3.2, ${}^{\mathcal{B}}\boldsymbol{\omega}, {}^{\mathcal{O}}\boldsymbol{\omega} \in \mathbb{R}^3$ represent the inertial angular velocity of the rigid satellite measured in the body-fixed frame and the inertial angular velocity of the orbit measured in the orbital frame respectively. With the use of the quaternion multiplication operator described in Equation 2.2, the error quaternion, $\boldsymbol{q}_e = \begin{bmatrix} q_{e0} & \boldsymbol{q}_{ev} \end{bmatrix}^T$ can then be formulated as:

$$\boldsymbol{q}_e = \boldsymbol{q}_{\mathcal{O}}^{-1} \otimes \boldsymbol{q}_{\mathcal{B}} \tag{3.3}$$

which can be expanded to:

$$\begin{bmatrix} q_{e0} \\ \boldsymbol{q}_{ev} \end{bmatrix} = \begin{bmatrix} {\boldsymbol{q}_{\mathcal{O}v}}^{T}\boldsymbol{q}_{\mathcal{B}v} + q_{\mathcal{B}v}q_{\mathcal{O}0} \\ q_{\mathcal{O}0}\boldsymbol{q}_{\mathcal{B}v} - \boldsymbol{q}_{\mathcal{O}v}^{\times}\boldsymbol{q}_{\mathcal{B}v} - q_{\mathcal{B}0}\boldsymbol{q}_{\mathcal{O}v} \end{bmatrix} \tag{3.4}$$

Similar to Equations 3.1 and 3.2, the error quaternion kinematics can then expressed as:

$$\begin{bmatrix} \dot{q}_{e0} \\ \dot{\boldsymbol{q}}_{ev} \end{bmatrix} = \begin{bmatrix} -\frac{1}{2}\boldsymbol{q}_{ev}^{T}\,{}^{\mathcal{B}}\boldsymbol{\omega}_e \\ \frac{1}{2}(q_{e0}I_3 + \boldsymbol{q}_{ev}^{\times})^{\mathcal{B}}\boldsymbol{\omega}_e \end{bmatrix} \tag{3.5}$$

where the error angular velocity, ${}^{\mathcal{B}}\boldsymbol{\omega}_e$, can then be expressed as:

$$ {}^{\mathcal{B}}\boldsymbol{\omega}_e = {}^{\mathcal{B}}\boldsymbol{\omega} - R_{\mathcal{B}\mathcal{O}}{}^{\mathcal{O}}\boldsymbol{\omega} \tag{3.6} $$

where $R_{\mathcal{B}\mathcal{O}} \in \mathbb{R}^{3x3}$ is the quaternion rotation matrix given in terms of the error quaternion that maps vectors from the orbital frame to the body-fixed frame. It is given by:

$$ R_{\mathcal{B}\mathcal{O}} = (q_{e0}^2 - \boldsymbol{q}_{ev}^T\boldsymbol{q}_{ev})I_3 + 2\boldsymbol{q}_{ev}\boldsymbol{q}_{ev}^T - 2q_{e0}\boldsymbol{q}_{ev}^{\times} \tag{3.7} $$

and can be expanded as:

$$ R_{\mathcal{B}\mathcal{O}} = \begin{bmatrix} 2q_{e0}^2 + 2q_{e1}^2 - 1 & 2q_{e1}q_{e2} + 2q_{e0}q_{e3} & 2q_{e1}q_{e3} - 2q_{e0}q_{e2} \\ 2q_{e1}q_{e2} - 2q_{e0}q_{e3} & 2q_{e0}^2 + 2q_{e2}^2 - 1 & 2q_{e3}q_{e2} + 2q_{e0}q_{e1} \\ 2q_{e1}q_{e3} + 2q_{e0}q_{e2} & 2q_{e2}q_{e3} - 2q_{e0}q_{e1} & 2q_{e0}^2 + 2q_{e3}^2 - 1 \end{bmatrix} \tag{3.8} $$

The error angular velocity term is important for the formulation of the error kinetics, and is also required for the sliding equation mentioned in the following sections.

3.3 The Two-Body Problem

Before discussing the kinetics of the satellite, a brief background to the gravitational interaction between the satellite and the Earth is provided in this subsection based on the two-body problem, which is extensively studied in classical mechanics and describes the motion of two bodies with respect to each other based on the attractive forces acting between them. Based on [30], in this thesis, the two-body problem is used to model a low-Earth circular orbit and to calculate the angular velocity vector of a satellite in that orbit due to the influence of Earth's gravitational force. In Figure 3.1, O is considered the origin of an inertial reference frame, m_1 to be the Earth and m_2 to be the satellite. The position vectors of the Earth and the satellite with respect to O are $\boldsymbol{R_1}$ and $\boldsymbol{R_2}$ respectively, whereas $\boldsymbol{R_{c.m}}$ is the position vector of the center of mass of the two-body system with respect to O. Since

$\boldsymbol{r} = \boldsymbol{R_2}$ - $\boldsymbol{R_1}$, it can be noted that $\ddot{\boldsymbol{r}} = \ddot{\boldsymbol{R}}_{\boldsymbol{2}}$ - $\ddot{\boldsymbol{R}}_{\boldsymbol{1}}$ and it follows from Newton's second and third law of motion that $\boldsymbol{F}_{12}$, the force that m_2 exerts on m_1, and $\boldsymbol{F}_{21}$, the force that m_1 exerts on m_2, are given by:

$$\boldsymbol{F_{12}} = m_1 \ddot{\boldsymbol{R}}_{\boldsymbol{1}} = \frac{G m_1 m_2}{r^3} \boldsymbol{r} \tag{3.9}$$

$$\boldsymbol{F_{21}} = m_2 \ddot{\boldsymbol{R}}_{\boldsymbol{2}} = -\frac{G m_2 m_1}{r^3} \boldsymbol{r} \tag{3.10}$$

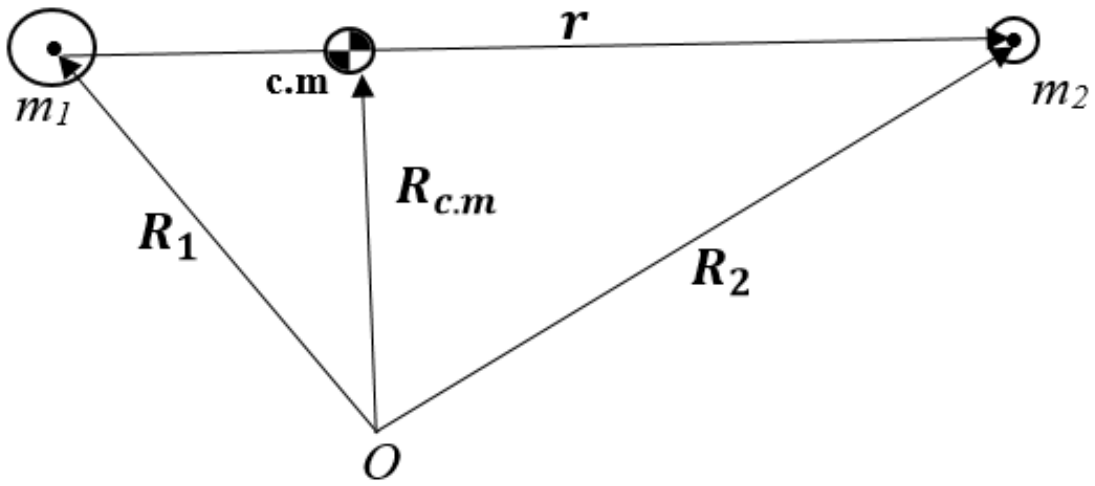

Figure 3.1 The Two-Body Problem

Since $\ddot{\boldsymbol{r}} = \ddot{\boldsymbol{R}}_{\boldsymbol{2}}$ - $\ddot{\boldsymbol{R}}_{\boldsymbol{1}}$, Equations (3.9) and (3.10) can be re-arranged in the following form:

$$\ddot{\boldsymbol{r}} = -\frac{\mu}{r^3} \boldsymbol{r} \tag{3.11}$$

where the gravitational parameter μ is given by $G(m_1 + m_2)$. The non-linear homogeneous differential equation in Equation (3.11) has a closed-form analytical solution given by:

$$r = \frac{h^2}{\mu} \frac{1}{1 + e \cos\theta} \tag{3.12}$$

which describes the motion of the body m_2 relative to m_1, where θ is the true anomaly, h

and e are the specific angular momentum and eccentricity of the orbit respectively. Using Equation (3.12), the satellite's motion in LEO can be modelled taking $e = 0$, since a circular orbit is considered in this study. Furthermore, the radial velocity in a circular orbit is zero as r does not change, and $h = vr = r^2\omega$. From this notion and from Equation 3.12, it can be shown that the speed ($v_{circular}$) and angular speed ($\omega_{circular}$) of a circular orbit are given by:

$$v_{circular} = \sqrt{\frac{\mu}{r}} \tag{3.13}$$

$$\omega_{circular} = \sqrt{\frac{\mu}{r^3}} \tag{3.14}$$

Based on these equations, it is understood that the inertial angular velocity of the orbit in orbital frame components is given by:

$$^{O}\boldsymbol{\omega} = \sqrt{\frac{\mu}{r^3}}\hat{k}' \tag{3.15}$$

where $r = R_E + h$ and $R_E = 6378km$ - the radius of the Earth, h is the altitude of the orbit, and $\hat{k}'$ is the unit normal to the plane of the circular orbit represented in Figure 3.2. The satellite's desired angular velocity is also given by Equation 3.15 to ensure that the satellite's body-fixed axes align with the orbital frame's axes. To satisfy the control goal of this study, which is to guarantee the satellite's Earth-pointing capability at all times, the on-board camera of the satellite can be positioned along the $-\hat{i}'$ direction.

3.4 Satellite Kinetics

Earth-pointing satellites and spacecraft are of common interest in aerospace applications, especially in Low-Earth orbits (LEO). They serve a multitude of purposes that extend to Earth-observation, navigation, security, scientific research and communications. However, maintaining an Earth-pointing attitude in LEO is generally difficult due to the dynamic environment presented by gravitational torques, atmospheric drag, radiation pressure and

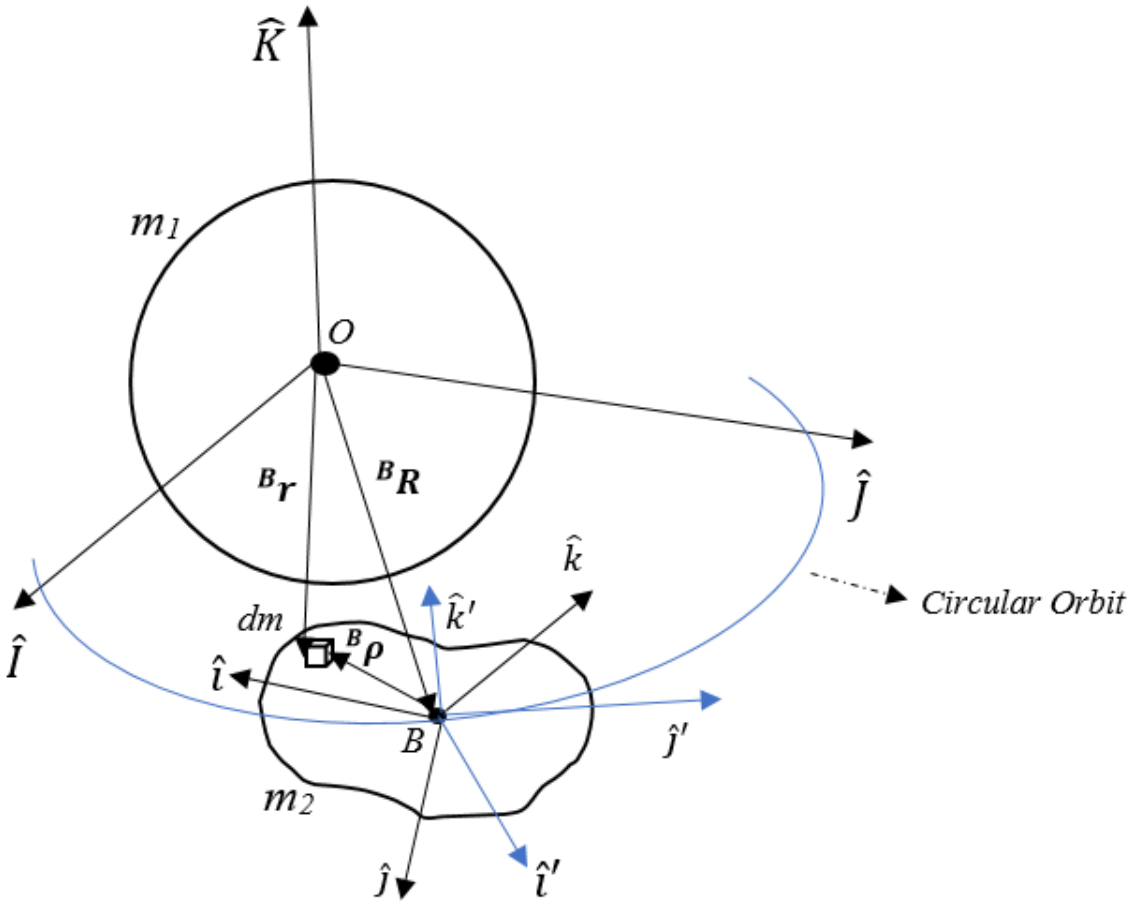

Figure 3.2 Rigid Satellite in a Circular Orbit

strong magnetic fields. Control effort is constantly required to ensure the stability of the Earth-pointing spacecraft system. However, with a detailed approach to the mathematical modeling of the kinematics and kinetics of the satellite system, the control laws can be developed such that the error quaternion tends to identity and error angular velocities tend to zero. Figure 3.2 provides a diagrammatic representation of a rigid satellite in an equatorial LEO and provides scope to understand the kinetics and Euler's equations of rotational motion. In the figure, the Earth-Centered Inertial Frame is denoted by the axes with unit vectors given by $\begin{bmatrix} \hat{I} & \hat{J} & \hat{K} \end{bmatrix}^T$. The rigid satellite body-fixed frame is denoted by the axes

with the unit vectors given by $\begin{bmatrix} \hat{i} & \hat{j} & \hat{k} \end{bmatrix}^T$. The orbital frame is represented by the axes where the unit vectors are given by $\begin{bmatrix} \hat{i}' & \hat{j}' & \hat{k}' \end{bmatrix}^T$ and the orbital frame is shown to have an x-axis unit vector pointing radially away from the Earth. The satellite's body-fixed axes and the orbital frame axes are shown to be misaligned initially. ${}^{\mathcal{B}}\mathbf{R}$ denotes the position vector of the satellite center of mass relative to the inertial frame. ${}^{\mathcal{B}}\mathbf{r}$ denotes the position vector of an infinitesimal mass element on the rigid satellite and ${}^{\mathcal{B}}\boldsymbol{\rho}$ is the position vector of the infinitesimal mass element dm relative to the satellite center of mass.

$$ {}^{\mathcal{B}}\mathbf{r} = {}^{\mathcal{B}}\boldsymbol{\rho} + {}^{\mathcal{B}}\mathbf{R} \tag{3.16} $$

where ${}^{\mathcal{B}}\boldsymbol{\rho}$ can be taken as follows:

$$ {}^{\mathcal{B}}\boldsymbol{\rho} = x_1\hat{i} + y_1\hat{j} + z_1\hat{k} \tag{3.17} $$

Taking the derivative of both sides of Equation (3.16) and invoking the transport theorem in mechanics leads to:

$$ {}^{\mathcal{B}}\dot{\boldsymbol{r}} = {}^{\mathcal{B}}\dot{\boldsymbol{\rho}} + ({}^{\mathcal{B}}\boldsymbol{\omega} \times {}^{\mathcal{B}}\boldsymbol{\rho}) + {}^{\mathcal{B}}\dot{\boldsymbol{R}} \tag{3.18} $$

Since the satellite is modelled as a rigid body, ${}^{\mathcal{B}}\dot{\boldsymbol{\rho}} = 0$. The angular momentum of an infinitesimal mass dm about the origin of the satellite's body-fixed axes (B) can be expressed as:

$$ {}^{\mathcal{B}}\boldsymbol{dh} = ({}^{\mathcal{B}}\boldsymbol{\rho} \times {}^{\mathcal{B}}\dot{\boldsymbol{r}})dm \tag{3.19} $$

Then, from Equation (3.18),

$$ {}^{\mathcal{B}}\boldsymbol{dh} = \Big({}^{\mathcal{B}}\boldsymbol{\rho} \times ({}^{\mathcal{B}}\dot{\boldsymbol{R}} + {}^{\mathcal{B}}\boldsymbol{\omega} \times {}^{\mathcal{B}}\boldsymbol{\rho})\Big)dm \tag{3.20} $$

The total angular momentum of the satellite about its c.m is then:

$$^{\mathcal{B}}\boldsymbol{h} = \int {}^{\mathcal{B}}\boldsymbol{\rho} \times ({}^{\mathcal{B}}\boldsymbol{\omega} \times {}^{\mathcal{B}}\boldsymbol{\rho})\, dm \tag{3.21}$$

$\int {}^{\mathcal{B}}\boldsymbol{\rho}\, dm \times {}^{\mathcal{B}}\dot{\boldsymbol{R}} = 0$ since the location of the c.m relative to itself is zero. Upon expansion of Equation (3.21) and the assumption that the body-fixed frame axes are aligned with the principal axes of inertia of the satellite and that the satellite has a uniform mass distribution, and from Equation (3.17), the total angular momentum of the body about its c.m can be expressed in its vector form as:

$$^{\mathcal{B}}\boldsymbol{h} = J^{\mathcal{B}}\boldsymbol{\omega} \tag{3.22}$$

where,

$$J = \begin{bmatrix} J_1 & 0 & 0 \\ 0 & J_2 & 0 \\ 0 & 0 & J_3 \end{bmatrix} \tag{3.23}$$

and,

$$J_1 = \int_{m_2} (y_1^2 + z_1^2)\, dm \tag{3.24}$$

$$J_2 = \int_{m_2} (x_1^2 + z_1^2)\, dm \tag{3.25}$$

$$J_3 = \int_{m_2} (x_1^2 + y_1^2)\, dm \tag{3.26}$$

Now, Euler's rotational dynamics states that the sum of the external torques acting on a rigid body is equivalent to the rate of change of angular momentum of the body. Therefore, by invoking the transport theorem in mechanics and taking the derivative of Equation 3.22, it can be noted that, in the presence of external disturbances and and control torques, the equations of motion of an inertial pointing rigid satellite can be expressed as:

$$J^{\mathcal{B}}\dot{\boldsymbol{\omega}} = -{}^{\mathcal{B}}\boldsymbol{\omega}^{\times} J^{\mathcal{B}}\boldsymbol{\omega} + \boldsymbol{u} + \boldsymbol{d} \tag{3.27}$$

where $J \in \mathbb{R}^{3x3}$ is the moment of inertia matrix of the rigid body, $\boldsymbol{u} \in \mathbb{R}^3$ is the control input, $\boldsymbol{d} \in \mathbb{R}^3$ is the external disturbances, and ${}^{\mathcal{B}}\boldsymbol{\omega}$ is the inertial angular velocity of the rigid satellite measured in the body-fixed frame, which can be expressed based on the re-arrangement of Equation 3.6 as:

$$ {}^{\mathcal{B}}\boldsymbol{\omega} = {}^{\mathcal{B}}\boldsymbol{\omega}_e + R_{\mathcal{B}\mathcal{O}}{}^{\mathcal{O}}\boldsymbol{\omega} \tag{3.28} $$

Now, taking the derivative of Equation 3.28, it can be noted that:

$$ {}^{\mathcal{B}}\dot{\boldsymbol{\omega}} = {}^{\mathcal{B}}\dot{\boldsymbol{\omega}}_e + R_{\mathcal{B}\mathcal{O}}{}^{\mathcal{O}}\dot{\boldsymbol{\omega}} + \dot{R}_{\mathcal{B}\mathcal{O}}{}^{\mathcal{O}}\boldsymbol{\omega} \tag{3.29} $$

which can then be expressed based on the transport theorem in mechanics, noting that $\dot{R}_{\mathcal{B}\mathcal{O}} = -{}^{\mathcal{B}}\boldsymbol{\omega}_e^{\times} R_{\mathcal{B}\mathcal{O}}$, ${}^{\mathcal{B}}\dot{\boldsymbol{\omega}}$ becomes:

$$ {}^{\mathcal{B}}\dot{\boldsymbol{\omega}} = {}^{\mathcal{B}}\dot{\boldsymbol{\omega}}_e + R_{\mathcal{B}\mathcal{O}}{}^{\mathcal{O}}\dot{\boldsymbol{\omega}} - {}^{\mathcal{B}}\boldsymbol{\omega}_e^{\times} R_{\mathcal{B}\mathcal{O}}{}^{\mathcal{O}}\boldsymbol{\omega} \tag{3.30} $$

It can be noted that the ${}^{\mathcal{O}}\dot{\boldsymbol{\omega}} = 0$ in the case of a circular orbit. Also, if it can be considered that ${}^{\mathcal{B}}\boldsymbol{\omega}_{\mathcal{O}} = R_{\mathcal{B}\mathcal{O}}{}^{\mathcal{O}}\boldsymbol{\omega}$, and upon the substitution of Equation 3.30 in Equation 3.27, the rigid satellite dynamics can be expressed in terms of the error angular velocity described in Equation 3.6 as:

$$ J{}^{\mathcal{B}}\dot{\boldsymbol{\omega}}_e = -({}^{\mathcal{B}}\boldsymbol{\omega}_e + R_{\mathcal{B}\mathcal{O}}{}^{\mathcal{O}}\boldsymbol{\omega})^{\times} J({}^{\mathcal{B}}\boldsymbol{\omega}_e + R_{\mathcal{B}\mathcal{O}}{}^{\mathcal{O}}\boldsymbol{\omega}) + J({}^{\mathcal{B}}\boldsymbol{\omega}_e^{\times} R_{\mathcal{B}\mathcal{O}}{}^{\mathcal{O}}\boldsymbol{\omega}) + \boldsymbol{u} + \boldsymbol{d} \tag{3.31} $$

By considering the error dynamics and kinematics, the attitude tracking problem can then be considered as an attitude stabilization problem. Equations 3.31 and 3.5 will be used for the design of the equivalent control term.

4 Control Design and Stability Analysis

4.1 Conventional Sliding Mode Controller Design

There are two main steps in the SMC design process - sliding manifold design and the selection of the control law. The sliding equation is selected based on the references in [31, 32] as:

$$\boldsymbol{s} = {}^{\mathcal{B}}\boldsymbol{\omega}_e + G\boldsymbol{q}_{ev} \tag{4.1}$$

where $\boldsymbol{s} \in \mathbb{R}^3$ and $G = G^T \in \mathbb{R}^{3\times3}$ is a positive-definite diagonal matrix. The sliding manifold is expressed by $\boldsymbol{s} = 0$. Using the sliding equation, the equivalent control can then be found by satisfying $\dot{\boldsymbol{s}} = {}^{\mathcal{B}}\dot{\boldsymbol{\omega}}_e + G\dot{\boldsymbol{q}}_{ev} = 0$ under the absence of the external disturbances. Therefore, from substitution of the error quaternion kinematics in Equation 3.5 and the error dynamics in Equation 3.31, the equivalent control can be expressed as:

$$\boldsymbol{u_{eq}} = ({}^{\mathcal{B}}\boldsymbol{\omega}_e + R_{\mathcal{B}\mathcal{O}}{}^{\mathcal{O}}\boldsymbol{\omega})^{\times} J({}^{\mathcal{B}}\boldsymbol{\omega}_e + R_{\mathcal{B}\mathcal{O}}{}^{\mathcal{O}}\boldsymbol{\omega}) - J({}^{\mathcal{B}}\boldsymbol{\omega}_e^{\times} R_{\mathcal{B}\mathcal{O}}{}^{\mathcal{O}}\boldsymbol{\omega}) - GJ\dot{\boldsymbol{q}}_{ev} \tag{4.2}$$

In conventional SMC, the discontinuous control term is given by:

$$\boldsymbol{u_{dsc}} = -U_{max}\,\mathrm{sgn}(\boldsymbol{s}) \tag{4.3}$$

where $U_{max} = U_{max}^T \in \mathbb{R}^{3\times3}$ is a constant positive-definite diagonal matrix in this case since $\boldsymbol{s} \in \mathbb{R}^3$.

The control law is then given by:

$$\boldsymbol{u} = \boldsymbol{u_{eq}} + \boldsymbol{u_{dsc}} \tag{4.4}$$

The reaching condition stated earlier in Equation 2.6 is critical in proving the existence of the sliding mode and can be satisfied through the selection of a suitable Lyapunov function.

The chosen Lyapunov function candidate is:

$$V = \frac{1}{2}\boldsymbol{s}^T J \boldsymbol{s} \tag{4.5}$$

where J is the moment of inertia matrix given by Equation 3.23. Since J is diagonal and $\boldsymbol{s}^T\boldsymbol{s} = \|\boldsymbol{s}\|_2^2$, the Lyapunov function V can be bounded as:

$$\lambda_{min}(J)\,\|\boldsymbol{s}\|_2^2 \leq \boldsymbol{s}^T J \boldsymbol{s} \leq \lambda_{max}(J)\,\|\boldsymbol{s}\|_2^2 \tag{4.6}$$

where $\lambda_{min}(J), \lambda_{max}(J)$ are the minimum and maximum eigenvalues of J respectively, which are equivalent to $\min(J)$ and $\max(J)$ due to the diagonal nature of J.

Before delving into further detail within the Lyapunov analysis, the following useful lemmas can be noted:

***Lemma* 4.1**: **L1 - L2 Norm Inequality** - Theorem 3.8 from [33]

For all $\boldsymbol{x} \in \mathbb{R}^n$, it can be noted that:

$$\|\boldsymbol{x}\|_2 \leq \|\boldsymbol{x}\|_1 \leq \sqrt{n}\,\|\boldsymbol{x}\|_2 \tag{4.7}$$

where

$$\|\boldsymbol{x}\|_1 = \sum_{i=1}^{n} |\boldsymbol{x}_i| \tag{4.8}$$

$$\|\boldsymbol{x}\|_2 = \sqrt{\sum_{i=1}^{n} \boldsymbol{x}_i^2} \tag{4.9}$$

***Lemma* 4.2**: **Lyapunov Theory** - (Theorem 4.2 from [34])

Suppose that $V(\boldsymbol{x})$ is defined on $D \subset \mathbb{R}^n$ is a positive-definite function that is continuously differentiable and $\dot{V}(\boldsymbol{x})$ is a negative semi-definite function defined on $D \subset \mathbb{R}^n$ for any $\eta \in \mathbb{R}^+$

and $\alpha \in (0,1)$ such that:

$$\dot{V}(\boldsymbol{x}) + \eta V^{\alpha}(\boldsymbol{x}) \leq 0,\ \boldsymbol{x} \in D_0 \backslash \{0\} \tag{4.10}$$

where $D_0 \subset \mathbb{R}^n$ is a neighborhood around the origin such that any $V(\boldsymbol{x})$ starting from $D_0 \subset \mathbb{R}^n$ can reach $V(\boldsymbol{x}) \equiv 0$ in finite-time. Then, the origin is considered to be a finite-time stable equilibrium point and the reaching time (T_r) can be found as:

$$T_r \leq \frac{V^{(1-\alpha)}(\boldsymbol{x}_0)}{\eta(1-\alpha)} \tag{4.11}$$

where $V(\boldsymbol{x}_0)$ is the value of $V(\boldsymbol{x}_0)$ at the starting time t_0.

The derivative of the Lyapunov function in Equation 4.5 can be simplified and expressed as:

$$\dot{V} = \boldsymbol{s}^T J \dot{\boldsymbol{s}} \tag{4.12}$$

Since $\dot{\boldsymbol{s}} = {}^{\mathcal{B}}\dot{\boldsymbol{\omega}}_e + G\dot{\boldsymbol{q}}_{ev}$, the $\dot{V}$ term can be simplified using the error quaternion kinematics and dynamics as:

$$\begin{aligned}
\dot{V} &= \boldsymbol{s}^T J({}^{\mathcal{B}}\dot{\boldsymbol{\omega}}_e + G\dot{\boldsymbol{q}}_{ev}) \\
&= \boldsymbol{s}^T \Big(- ({}^{\mathcal{B}}\boldsymbol{\omega}_e + R_{\mathcal{B}\mathcal{O}}{}^{\mathcal{O}}\boldsymbol{\omega})^{\times} J({}^{\mathcal{B}}\boldsymbol{\omega}_e + R_{\mathcal{B}\mathcal{O}}{}^{\mathcal{O}}\boldsymbol{\omega}) + J({}^{\mathcal{B}}\boldsymbol{\omega}_e^{\times} R_{\mathcal{B}\mathcal{O}}{}^{\mathcal{O}}\boldsymbol{\omega}) + \boldsymbol{u} + \boldsymbol{d} + GJ\dot{\boldsymbol{q}}_{ev} \Big) \\
&= \boldsymbol{s}^T \Big(- ({}^{\mathcal{B}}\boldsymbol{\omega}_e + R_{\mathcal{B}\mathcal{O}}{}^{\mathcal{O}}\boldsymbol{\omega})^{\times} J({}^{\mathcal{B}}\boldsymbol{\omega}_e + R_{\mathcal{B}\mathcal{O}}{}^{\mathcal{O}}\boldsymbol{\omega}) + J({}^{\mathcal{B}}\boldsymbol{\omega}_e^{\times} R_{\mathcal{B}\mathcal{O}}{}^{\mathcal{O}}\boldsymbol{\omega}) + \boldsymbol{u}_{eq} + \boldsymbol{u}_{\boldsymbol{dsc}} + \boldsymbol{d} + GJ\dot{\boldsymbol{q}}_{ev} \Big) \\
&= \boldsymbol{s}^T \Big(- ({}^{\mathcal{B}}\boldsymbol{\omega}_e + R^{\mathcal{O}}\boldsymbol{\omega})^{\times} J({}^{\mathcal{B}}\boldsymbol{\omega}_e + R_{\mathcal{B}\mathcal{O}}{}^{\mathcal{O}}\boldsymbol{\omega}) + J({}^{\mathcal{B}}\boldsymbol{\omega}_e^{\times} R_{\mathcal{B}\mathcal{O}}{}^{\mathcal{O}}\boldsymbol{\omega}) + GJ\dot{\boldsymbol{q}}_{ev} \\
&\quad + ({}^{\mathcal{B}}\boldsymbol{\omega}_e + R_{\mathcal{B}\mathcal{O}}{}^{\mathcal{O}}\boldsymbol{\omega})^{\times} J({}^{\mathcal{B}}\boldsymbol{\omega}_e + R_{\mathcal{B}\mathcal{O}}{}^{\mathcal{O}}\boldsymbol{\omega}) - J({}^{\mathcal{B}}\boldsymbol{\omega}_e^{\times} R_{\mathcal{B}\mathcal{O}}{}^{\mathcal{O}}\boldsymbol{\omega}) - GJ\dot{\boldsymbol{q}}_{ev} - U_{\max}\operatorname{sgn}(\boldsymbol{s}) \\
&\quad + \boldsymbol{d} + GJ\dot{\boldsymbol{q}}_{ev} \Big) \\
&= \boldsymbol{s}^T \Big(- U_{\max}\operatorname{sgn}(\boldsymbol{s}) + \boldsymbol{d} \Big)
\end{aligned} \tag{4.13}$$

Let the disturbance be upper-bounded such that:

$$\|\boldsymbol{d}\|_2 \leq d_o \tag{4.14}$$

Noting that $\boldsymbol{s}^T(-U_{\max}\,\mathrm{sgn}(\boldsymbol{s})) = \sum_{i=1}^{3} -U_{\max}\,|\boldsymbol{s}_i| = \|\boldsymbol{s}\|_1$ and $\boldsymbol{s}^T\boldsymbol{d} \leq \|\boldsymbol{s}\|_2\,\|\boldsymbol{d}\|_2$, Equation 4.13 becomes:

$$\begin{aligned}
\dot{V} &\leq \sum_{i=1}^{3} -U_{\max}\,|\boldsymbol{s}_i| + \|\boldsymbol{s}\|_2\,\|\boldsymbol{d}\|_2 \\
&= -U_{\max}\,\|\boldsymbol{s}\|_1 + \|\boldsymbol{s}\|_2\,\|\boldsymbol{d}\|_2 \\
&\leq -U_{\max}\,\|\boldsymbol{s}\|_1 + \|\boldsymbol{s}\|_2\,(\|\boldsymbol{d}\|_2 - d_0) \\
&\leq -U_{\max}\,\|\boldsymbol{s}\|_1
\end{aligned} \tag{4.15}$$

To analyze the existence of sliding mode and the finite-time convergence of the states to the sliding manifold, it can be noted from Equation 4.6 and the fact that J is a symmetrical matrix that:

$$\sqrt{\frac{2V}{\lambda_{max}(J)}} \leq \|\boldsymbol{s}\|_2 \leq \sqrt{\frac{2V}{\lambda_{min}(J)}} \tag{4.16}$$

Invoking *Lemma* 4.1, $\|\boldsymbol{s}\|_1$ and $\|\boldsymbol{s}\|_2$ can be related by:

$$\|\boldsymbol{s}\|_1 \geq \|\boldsymbol{s}\|_2 \tag{4.17}$$

From Equation 4.16 it can be noted that:

$$\|\boldsymbol{s}\|_2 \geq \sqrt{\frac{2V}{\lambda_{max}(J)}} \tag{4.18}$$

Therefore,

$$\dot{V} \leq -U_{\max}\,\|\boldsymbol{s}\|_1 \leq -U_{\max}\,\|\boldsymbol{s}\|_2 \leq -U_{\max}\sqrt{\frac{2V}{\lambda_{max}(J)}} \tag{4.19}$$

Now, invoking *Lemma* 4.2, Equation 4.19 can be expressed as:

$$\dot{V} + \eta V^{\alpha} \leq 0 \tag{4.20}$$

where, $\eta = U_{\max}\sqrt{\frac{2}{\lambda_{max}(J)}}$ and $\alpha = 0.5$. This result implies that the trajectory of the closed-loop system given by Equations 3.5 and 3.31 will reach the sliding manifold $\boldsymbol{s} = 0$ in finite-time given by:

$$T_r \leq \frac{V^{\frac{1}{2}}(\boldsymbol{s}_0)}{U_{\max}\sqrt{\frac{2}{\lambda_{max}(J)}}} \tag{4.21}$$

4.2 Adaptive Controller

Since it was assumed that the error angular velocity and error quaternion measurements are available, an adaptive controller is designed for the attitude tracking of the satellite. A disturbance estimation, $\hat{\boldsymbol{d}}$, is performed based on Lyapunov analysis. The control structure is as follows:

$$\boldsymbol{u} = \boldsymbol{u_{inv}} + \boldsymbol{u_{fb}} \tag{4.22}$$

where the inverse dynamics control term, $\boldsymbol{u}_{inv}$ is given by:

$$\boldsymbol{u_{inv}} = ({}^{\mathcal{B}}\boldsymbol{\omega}_e + R_{\mathcal{B}\mathcal{O}}{}^{\mathcal{O}}\boldsymbol{\omega})^{\times} J({}^{\mathcal{B}}\boldsymbol{\omega}_e + R_{\mathcal{B}\mathcal{O}}{}^{\mathcal{O}}\boldsymbol{\omega}) - J({}^{\mathcal{B}}\boldsymbol{\omega}_e^{\times} R_{\mathcal{B}\mathcal{O}}{}^{\mathcal{O}}\boldsymbol{\omega}) - GJ\dot{\boldsymbol{q}}_{ev} - \hat{\boldsymbol{d}} \tag{4.23}$$

where $\hat{\boldsymbol{d}} \in \mathbb{R}^3$ is the disturbance estimation term and $\boldsymbol{u_{fb}}$ is given by:

$$\boldsymbol{u_{fb}} = -K\boldsymbol{s} \tag{4.24}$$

where $\boldsymbol{s}$ is given by Equation 4.1 and $K = K^T \in \mathbb{R}^{3\times3}$ is a positive-definite diagonal gain matrix.

To verify the validity of the control design, the Lyapunov function can be considered as follows:

$$V = \frac{1}{2}\boldsymbol{s}^T J \boldsymbol{s} + \frac{1}{2}\tilde{\boldsymbol{d}}^T \tilde{\boldsymbol{d}} \tag{4.25}$$

where $\tilde{\boldsymbol{d}}$ is defined as:

$$\tilde{\boldsymbol{d}} = \hat{\boldsymbol{d}} - \boldsymbol{d} \tag{4.26}$$

It can be noted that $\dot{\tilde{\boldsymbol{d}}} = \dot{\hat{\boldsymbol{d}}}$ in the presence of constant disturbance $\boldsymbol{d}$. Taking the derivative of the Lyapunov function in Equation 4.25, $\dot{V}$ can be obtained as:

$$\begin{aligned}
\dot{V} &= \boldsymbol{s}^T J({}^{\mathcal{B}}\dot{\boldsymbol{\omega}}_e + G\dot{\boldsymbol{q}}_{ev}) + \tilde{\boldsymbol{d}}^T \dot{\hat{\boldsymbol{d}}} \\
&= \boldsymbol{s}^T \Big(- ({}^{\mathcal{B}}\boldsymbol{\omega}_e + R_{\mathcal{B}\mathcal{O}}{}^{\mathcal{O}}\boldsymbol{\omega})^{\times} J({}^{\mathcal{B}}\boldsymbol{\omega}_e + R_{\mathcal{B}\mathcal{O}}{}^{\mathcal{O}}\boldsymbol{\omega}) + J({}^{\mathcal{B}}\boldsymbol{\omega}_e^{\times} R_{\mathcal{B}\mathcal{O}}{}^{\mathcal{O}}\boldsymbol{\omega}) + \boldsymbol{u} + \boldsymbol{d} + GJ\dot{\boldsymbol{q}}_{ev} \Big) \\
&\quad + \tilde{\boldsymbol{d}}^T \dot{\hat{\boldsymbol{d}}} \\
&= \boldsymbol{s}^T \Big(- ({}^{\mathcal{B}}\boldsymbol{\omega}_e + R_{\mathcal{B}\mathcal{O}}{}^{\mathcal{O}}\boldsymbol{\omega})^{\times} J({}^{\mathcal{B}}\boldsymbol{\omega}_e + R_{\mathcal{B}\mathcal{O}}{}^{\mathcal{O}}\boldsymbol{\omega}) + J({}^{\mathcal{B}}\boldsymbol{\omega}_e^{\times} R_{\mathcal{B}\mathcal{O}}{}^{\mathcal{O}}\boldsymbol{\omega}) + \boldsymbol{u}_{inv} + \boldsymbol{u}_{fb} + \boldsymbol{d} + GJ\dot{\boldsymbol{q}}_{ev} \Big) \\
&\quad + \tilde{\boldsymbol{d}}^T \dot{\hat{\boldsymbol{d}}} \\
&= \boldsymbol{s}^T \Big(- ({}^{\mathcal{B}}\boldsymbol{\omega}_e + R_{\mathcal{B}\mathcal{O}}{}^{\mathcal{O}}\boldsymbol{\omega})^{\times} J({}^{\mathcal{B}}\boldsymbol{\omega}_e + R_{\mathcal{B}\mathcal{O}}{}^{\mathcal{O}}\boldsymbol{\omega}) + J({}^{\mathcal{B}}\boldsymbol{\omega}_e^{\times} R_{\mathcal{B}\mathcal{O}}{}^{\mathcal{O}}\boldsymbol{\omega}) \\
&\quad + ({}^{\mathcal{B}}\boldsymbol{\omega}_e + R_{\mathcal{B}\mathcal{O}}{}^{\mathcal{O}}\boldsymbol{\omega})^{\times} J({}^{\mathcal{B}}\boldsymbol{\omega}_e + R_{\mathcal{B}\mathcal{O}}{}^{\mathcal{O}}\boldsymbol{\omega}) - J({}^{\mathcal{B}}\boldsymbol{\omega}_e^{\times} R_{\mathcal{B}\mathcal{O}}{}^{\mathcal{O}}\boldsymbol{\omega}) - GJ\dot{\boldsymbol{q}}_{ev} - \hat{\boldsymbol{d}} - K\boldsymbol{s} + \boldsymbol{d} + GJ\dot{\boldsymbol{q}}_{ev} \Big) \\
&\quad + \tilde{\boldsymbol{d}}^T \dot{\hat{\boldsymbol{d}}} \\
&= \boldsymbol{s}^T(-\tilde{\boldsymbol{d}} - K\boldsymbol{s}) + \tilde{\boldsymbol{d}}^T \dot{\hat{\boldsymbol{d}}} \\
&= -\tilde{\boldsymbol{d}}^T \boldsymbol{s} - \boldsymbol{s}^T K \boldsymbol{s} + \tilde{\boldsymbol{d}}^T \dot{\hat{\boldsymbol{d}}}
\end{aligned} \tag{4.27}$$

If it can be considered that:

$$\dot{\hat{\boldsymbol{d}}} = \boldsymbol{s} \tag{4.28}$$

then, Equation 4.27 becomes:

$$\dot{V} = -\boldsymbol{s}^T K \boldsymbol{s} \leq 0 \tag{4.29}$$

Now, by invoking Barbalat's Lemma, it can be noted that if $\ddot{V}(\boldsymbol{x}, t)$ is bounded, then

$\lim_{t\to\infty} \dot{V}(\boldsymbol{x}, t) \to 0$. To verify this condition, $\ddot{V}$ is:

$$\begin{aligned}
\ddot{V} &= -2\boldsymbol{s}^T K \dot{\boldsymbol{s}} \\
&= -2\boldsymbol{s}^T K({}^{\mathcal{B}}\dot{\boldsymbol{\omega}}_e + G\dot{\boldsymbol{q}}_{ev}) \\
&= -2\boldsymbol{s}^T K\Big(- ({}^{\mathcal{B}}\boldsymbol{\omega}_e + R_{\mathcal{B}\mathcal{O}}{}^{\mathcal{O}}\boldsymbol{\omega})^{\times} J({}^{\mathcal{B}}\boldsymbol{\omega}_e + R_{\mathcal{B}\mathcal{O}}{}^{\mathcal{O}}\boldsymbol{\omega}) + J({}^{\mathcal{B}}\boldsymbol{\omega}_e^{\times} R_{\mathcal{B}\mathcal{O}}{}^{\mathcal{O}}\boldsymbol{\omega}) + \boldsymbol{u} + \boldsymbol{d}\Big) \\
&\quad + 2\boldsymbol{s}^T K G \dot{\boldsymbol{q}}_{ev}
\end{aligned} \tag{4.30}$$

Upon substitution of $\boldsymbol{u}$ from Equation 4.22 $\ddot{V}$ becomes:

$$\ddot{V} = -2\boldsymbol{s}^T K \boldsymbol{s} + 2\boldsymbol{s}^T K \tilde{\boldsymbol{d}} \tag{4.31}$$

It can be noted that $\boldsymbol{s}$ and $\tilde{\boldsymbol{d}}$ are bounded by the Lyapunov analysis from Equation 4.29. Therefore, from the Lyapunov Direct Method and Barbalat's Lemma, it can be concluded that the error angular velocity ($\boldsymbol{\omega}_e$) and the vector component of the error quaternion ($\boldsymbol{q}_{ev}$) will asymptotically converge to zero with the implementation of the proposed adaptive controller.

4.3 Proposed Sliding Mode Controller with Disturbance Estimation

The proposed modification to the Sliding Mode Control strategy involves estimation of the constant disturbance term using Lyapunov analysis. The sliding equation is considered to be same as that used for the Conventional Sliding Mode Control design stated in Equation 4.1. The equivalent control term, $\boldsymbol{u}_{eq}$, is considered to be the same as $\boldsymbol{u}_{inv}$ from Equation 4.23 and is re-stated here as:

$$\boldsymbol{u_{eq}} = ({}^{\mathcal{B}}\boldsymbol{\omega}_e + R_{\mathcal{B}\mathcal{O}}{}^{\mathcal{O}}\boldsymbol{\omega})^{\times} J({}^{\mathcal{B}}\boldsymbol{\omega}_e + R_{\mathcal{B}\mathcal{O}}{}^{\mathcal{O}}\boldsymbol{\omega}) - J({}^{\mathcal{B}}\boldsymbol{\omega}_e^{\times} R_{\mathcal{B}\mathcal{O}}{}^{\mathcal{O}}\boldsymbol{\omega}) - GJ\dot{\boldsymbol{q}}_{ev} - \hat{\boldsymbol{d}} \tag{4.32}$$

where $\hat{\boldsymbol{d}} \in \mathbb{R}^3$ is the disturbance estimation term. It should be noted that the $\hat{\boldsymbol{d}}$ term in $\boldsymbol{u}_{eq}$ is included additionally after isolating $\boldsymbol{u}$ from $\dot{\boldsymbol{s}} = 0$.

To carry out the control design and perform the stability analysis, the candidate Lyapunov function is again chosen as:

$$V = \frac{1}{2}\boldsymbol{s}^T J \boldsymbol{s} + \frac{1}{2}\tilde{\boldsymbol{d}}^T \tilde{\boldsymbol{d}} \tag{4.33}$$

where, $\tilde{\boldsymbol{d}}$ is defined as:

$$\tilde{\boldsymbol{d}} = \hat{\boldsymbol{d}} - \boldsymbol{d} \tag{4.34}$$

It can further be noted that $\dot{\tilde{\boldsymbol{d}}} = \dot{\hat{\boldsymbol{d}}}$ in the presence of constant disturbance $\boldsymbol{d}$. Then, the derivative of the Lyapunov function stated in Equation 4.33 can be found as:

$$\begin{aligned}
\dot{V} &= \boldsymbol{s}^T J({}^{\mathcal{B}}\dot{\boldsymbol{\omega}}_e + G\dot{\boldsymbol{q}}_{ev}) + \tilde{\boldsymbol{d}}^T \dot{\hat{\boldsymbol{d}}} \\
&= \boldsymbol{s}^T \Big(-({}^{\mathcal{B}}\boldsymbol{\omega}_e + R_{\mathcal{B}\mathcal{O}}{}^{\mathcal{O}}\boldsymbol{\omega})^{\times} J({}^{\mathcal{B}}\boldsymbol{\omega}_e + R_{\mathcal{B}\mathcal{O}}{}^{\mathcal{O}}\boldsymbol{\omega}) + J({}^{\mathcal{B}}\boldsymbol{\omega}_e^{\times} R_{\mathcal{B}\mathcal{O}}{}^{\mathcal{O}}\boldsymbol{\omega}) + \boldsymbol{u} + \boldsymbol{d} + GJ\dot{\boldsymbol{q}}_{ev} \Big) + \tilde{\boldsymbol{d}}^T \dot{\hat{\boldsymbol{d}}} \\
&= \boldsymbol{s}^T \Big(-({}^{\mathcal{B}}\boldsymbol{\omega}_e + R_{\mathcal{B}\mathcal{O}}{}^{\mathcal{O}}\boldsymbol{\omega})^{\times} J({}^{\mathcal{B}}\boldsymbol{\omega}_e + R_{\mathcal{B}\mathcal{O}}{}^{\mathcal{O}}\boldsymbol{\omega}) + J({}^{\mathcal{B}}\boldsymbol{\omega}_e^{\times} R_{\mathcal{B}\mathcal{O}}{}^{\mathcal{O}}\boldsymbol{\omega}) + \boldsymbol{u}_{eq} + \boldsymbol{u}_{\boldsymbol{dsc}} + \boldsymbol{d} + GJ\dot{\boldsymbol{q}}_{ev} \Big) \\
&\quad + \tilde{\boldsymbol{d}}^T \dot{\hat{\boldsymbol{d}}}
\end{aligned} \tag{4.35}$$

Now, upon substitution of $\boldsymbol{u}_{\boldsymbol{dsc}}$ and $\boldsymbol{u}_{\boldsymbol{eq}}$ from Equations 4.3 and 4.32 respectively into the derivative of the Lyapunov function, it can be noted that:

$$\begin{aligned}
\dot{V} = \boldsymbol{s}^T \Big(& -({}^{\mathcal{B}}\boldsymbol{\omega}_e + R_{\mathcal{B}\mathcal{O}}{}^{\mathcal{O}}\boldsymbol{\omega})^{\times} J({}^{\mathcal{B}}\boldsymbol{\omega}_e + R_{\mathcal{B}\mathcal{O}}{}^{\mathcal{O}}\boldsymbol{\omega}) \\
& + J({}^{\mathcal{B}}\boldsymbol{\omega}_e^{\times} R_{\mathcal{B}\mathcal{O}}{}^{\mathcal{O}}\boldsymbol{\omega}) + ({}^{\mathcal{B}}\boldsymbol{\omega}_e + R_{\mathcal{B}\mathcal{O}}{}^{\mathcal{O}}\boldsymbol{\omega})^{\times} J({}^{\mathcal{B}}\boldsymbol{\omega}_e + R_{\mathcal{B}\mathcal{O}}{}^{\mathcal{O}}\boldsymbol{\omega}) \\
& - J({}^{\mathcal{B}}\boldsymbol{\omega}_e^{\times} R_{\mathcal{B}\mathcal{O}}{}^{\mathcal{O}}\boldsymbol{\omega}) - GJ\dot{\boldsymbol{q}}_{ev} - \hat{\boldsymbol{d}} - U_{\max}\,\mathrm{sgn}(\boldsymbol{s}) + \boldsymbol{d} + GJ\dot{\boldsymbol{q}}_{ev} \Big) \\
& + \tilde{\boldsymbol{d}}^T \dot{\hat{\boldsymbol{d}}}
\end{aligned} \tag{4.36}$$

Then, upon further simplification,

$$\dot{V} = \boldsymbol{s}^T \Big(\hat{\boldsymbol{d}} - U_{\max}\,\mathrm{sgn}(\boldsymbol{s}) + \boldsymbol{d} \Big) + \tilde{\boldsymbol{d}}^T \dot{\hat{\boldsymbol{d}}} \tag{4.37}$$

Now, from substitution of $\tilde{\boldsymbol{d}}$ from Equation 4.34, $\dot{V}$ can be expressed as:

$$\begin{aligned}\dot{V} &= \boldsymbol{s}^T\Big(-\tilde{\boldsymbol{d}} - U_{\max}\operatorname{sgn}(\boldsymbol{s})\Big) + \tilde{\boldsymbol{d}}^T\dot{\hat{\boldsymbol{d}}} \\ &= -\tilde{\boldsymbol{d}}^T\boldsymbol{s} - \boldsymbol{s}^T U_{\max}\operatorname{sgn}(\boldsymbol{s}) + \tilde{\boldsymbol{d}}^T\dot{\hat{\boldsymbol{d}}}\end{aligned} \tag{4.38}$$

If it can be again considered that:

$$\dot{\hat{\boldsymbol{d}}} = \boldsymbol{s} \tag{4.39}$$

then Equation $\dot{V}$ in 4.38 becomes:

$$\begin{aligned}\dot{V} &= -\boldsymbol{s}^T U_{\max}\operatorname{sgn}(\boldsymbol{s}) \\ &= \sum_{i=1}^{3} -U_{\max}\left|\boldsymbol{s}_i\right| \\ &= -U_{\max}\left\|\boldsymbol{s}\right\|_1 \\ &\leq -U_{\max}\left\|\boldsymbol{s}\right\|_2 \quad \text{(from Equation 4.7, } \left\|\boldsymbol{s}\right\|_1 \geq \left\|\boldsymbol{s}\right\|_2\text{)}\end{aligned} \tag{4.40}$$

If it can be considered that $\beta = \frac{\left\|\tilde{\boldsymbol{d}}\right\|_2^2}{2}$, then V from Equation 4.33 can be bounded such that:

$$\frac{\lambda_{min}(J)}{2}\left\|\boldsymbol{s}\right\|_2^2 + \beta_{max} \leq V \leq \frac{\lambda_{max}(J)}{2}\left\|\boldsymbol{s}\right\|_2^2 + \beta_{max} \tag{4.41}$$

which implies:

$$\left\|\boldsymbol{s}\right\|_2 \geq \sqrt{\frac{2V - 2\beta_{max}}{\lambda_{max}(J)}} \tag{4.42}$$

Now, from Equation 4.40:

$$\begin{aligned}\dot{V} &\leq -U_{\max}\left\|\boldsymbol{s}\right\|_2 \\ &\leq -U_{\max}\sqrt{\frac{2}{\lambda_{max}(J)}}\sqrt{V - \beta_{max}}\end{aligned} \tag{4.43}$$

Then, Equation 4.43 can be expressed as:

$$\dot{V} \leq -\eta\sqrt{V - \beta_{max}} \tag{4.44}$$

which can be expressed in the form:

$$\dot{\tilde{V}} + \eta\tilde{V}^{\alpha} \leq 0 \tag{4.45}$$

where $\tilde{V} = V - \beta_{max}$ with $\eta = U_{\max}\sqrt{\frac{2}{\lambda_{max}(J)}}$ and $\alpha = 0.5$, which is similar to the form given in Equation 4.10 from *Lemma* 4.2. Furthermore, to calculate the reaching time (T_r) based on Equation 4.45, it can be considered that:

$$\int_{V(\boldsymbol{s}_0)}^{\beta_{\max}} \frac{dV}{\eta\sqrt{V - \beta_{\max}}} = -\int_0^{T_r} dt \tag{4.46}$$

which then simplifies to

$$T_r \leq \frac{2\sqrt{V(\boldsymbol{s}_0) - \beta_{max}}}{\eta} \tag{4.47}$$

By virtue of *Lemma* 4.2, it can be noted that V converges to the residual set defined by β_{max}, and when V is close to β_{max}, the $\sqrt{V - \beta_{\max}}$ term becomes small, indicating that $\dot{V}$ also becomes small and V stabilizes around β_{max}. This further indicates that $\boldsymbol{s}$ will converge to a neighborhood around zero defined by β_{max}.

5 Simulation Framework

This section will provide details as to how the mathematical modeling of the kinematics, dynamics and control design were incorporated into MATLAB's Simulink environment. The blocks shown in the block diagrams in Figures 5.1, 5.2 represent subsystems in which the kinematic and dynamical equations from Section 3 are numerically integrated using MATLAB's Runge-Kutta solver with a fixed step time of $0.001s$ over the course of the simulation time to drive the error angular velocities to zero and the error quaternion to the identity quaternion using the controllers designed in Section 4.

5.1 Implementation of Conventional Sliding Mode Control

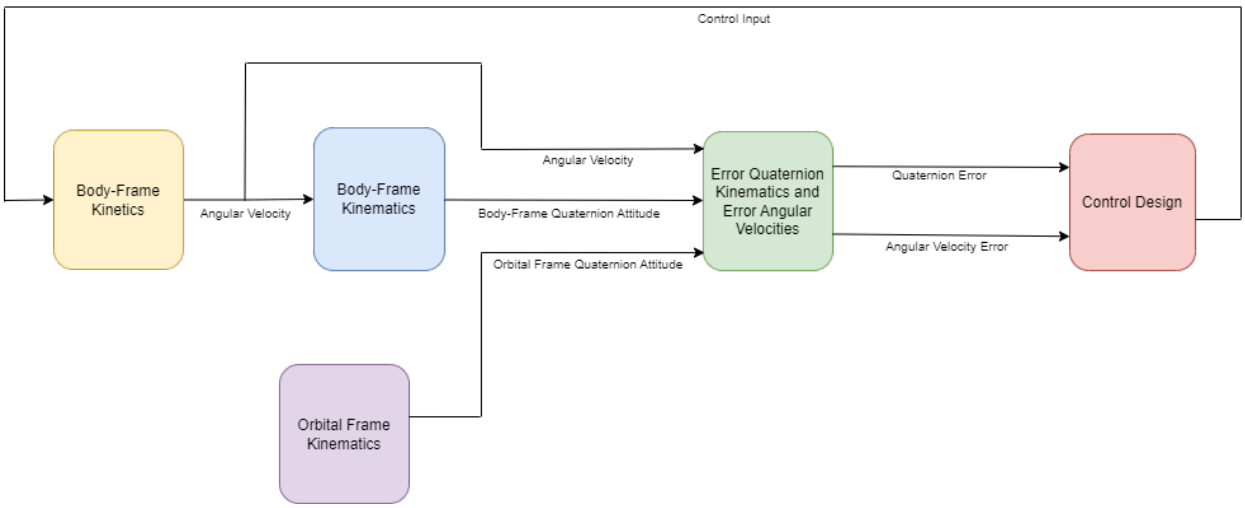

Figure 5.1 Block Diagram for Conventional Sliding Mode Control Implementation

Figure 5.1 shows the main block diagram created to implement the Conventional Sliding Mode Controller on the satellite. The Body-Frame Kinetics subsystem incorporates Equation 3.27, where the first-order differential equation is numerically integrated to obtain the body-frame angular velocity vector, ${}^{\mathcal{B}}\boldsymbol{\omega}$, which is then fed into the Body-Frame Kinematics subsystem. The first-order quaternion kinematic differential equation given by Equation 3.1 is solved to obtain the time-history of the body-quaternion, $\boldsymbol{q}_{\mathcal{B}}$. Similarly, the orbital-frame quaternion kinematics in Equation 3.2 are numerically integrated in the Orbital Frame Kine-

matics subsystem using the orbit angular velocity vector, ${}^{\mathcal{O}}\boldsymbol{\omega}$, described in Equation 3.15 to obtain $\boldsymbol{q}_{\mathcal{O}}$ - the orbit-frame quaternion. Both, $\boldsymbol{q}_{\mathcal{B}}$ and $\boldsymbol{q}_{\mathcal{O}}$ are fed into the Error Quaternion Kinematics and Error Angular Velocity subsystem, where the error quaternion, $\boldsymbol{q}_e$, is computed using Equation 3.3, incorporated in Equation 3.8 and subsequently in Equation 3.6 to calculate the error angular velocity vector, ${}^{B}\boldsymbol{\omega}_e$. The error quaternion and error angular velocity vectors are then fed into the Control Design subsystem, where they are used in Equation 4.1 to develop the sliding equation and the equivalent control $\boldsymbol{u_{eq}}$, using Equation 4.2. The control law is then developed based on Equation 4.4 and fed back into the Body-Frame Kinetics subsystem, where the disturbance term, $\boldsymbol{d} \in \mathbb{R}^3$, is selected to be a constant vector with an order of magnitude comparable to that experienced by small-satellites in LEO.

5.2 Implementation of Adaptive Control and Sliding Mode Control with Disturbance Estimation

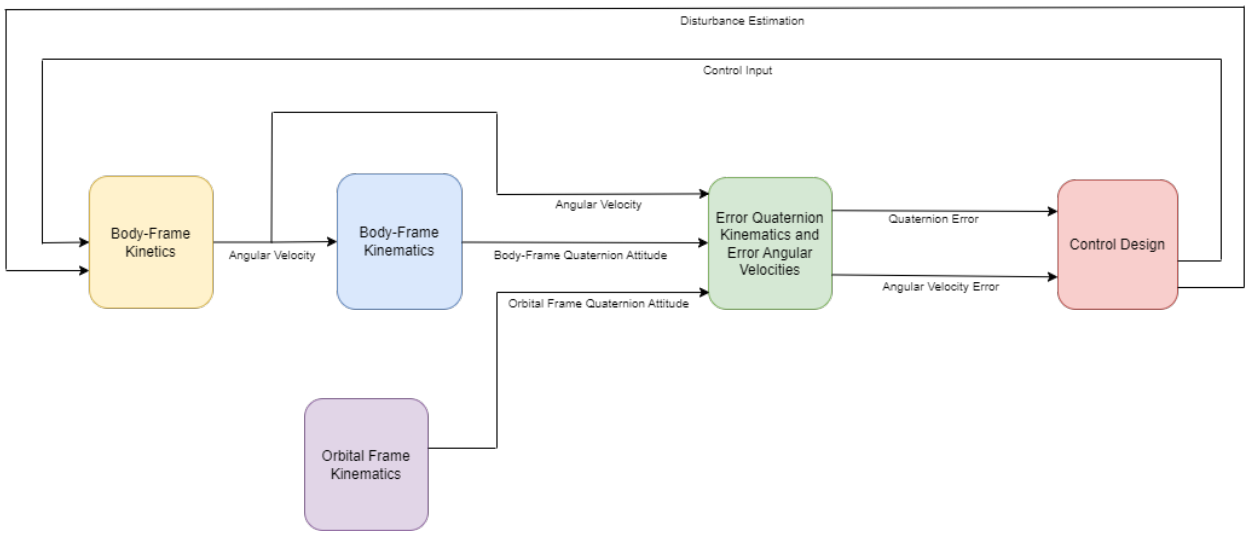

Figure 5.2 Block Diagram for Implementation of Adaptive Control and Sliding Mode Control with Disturbance Estimation

The block diagram for the Adaptive Controller and the Sliding Mode Controller with the Disturbance Estimation component remains similar to the block diagram designed for the Conventional Sliding Mode Controller. The only change involves the addition of an external loop for the disturbance estimation, where the dynamics are described by Equation 4.39 and

fed into the Body-Frame Kinetics Subsystem. In the case of the the Adaptive Controller, the Control Design subsystem incorporates the control law $\boldsymbol{u}$ from Equation 4.22, whereas the Sliding Mode Controller with the Disturbance Estimator incorporates the control law given by $\boldsymbol{u} = \boldsymbol{u_{eq}} + \boldsymbol{u_{dsc}}$, where $\boldsymbol{u_{eq}}$ comes from Equation 4.32 and $\boldsymbol{u_{dsc}}$ comes from Equation 4.3 and has smaller components of $U_{\max}$ when compared to the $\boldsymbol{u_{dsc}}$ used for the Conventional Sliding Mode Controller.

6 Results and Discussion

In this section, simulations are carried out based on two different cases of initial misalignment between the satellite body-fixed frame and the inertial frame to test the effectiveness of the controllers designed. Case 1 represents a 15° misalignment about an eigen-axis whereas Case 2 represents a 35° about a different eigen-axis. The details of the parameters that remain unchanged across both the cases are mentioned in Table 6.1. The orbital angular velocity is calculated using Equation 3.15, where $h = 400\ km$. The moment of inertia of the satellite is calculated based on a standard 3U CubeSat with dimensions 0.1 m × 0.1 m × 0.3 m. The gain matrix, G, from Equation 4.1 and the gain matrix, K, from Equation 4.24 in the adaptive controller design were unchanged, and $U_{\max}$ for the Conventional Sliding Mode Controller was unchanged for the two cases of simulations performed. The disturbance torque considered was of the same order of magnitude as that experienced by a spacecraft in LEO.

Table 6.1 Numerical Simulation Parameters

Parameter Name	Value
Gravitational Parameter	398600 km^3/s^2
Satellite Moment of Inertia	$\begin{bmatrix} 0.0083 & 0 & 0 \\ 0 & 0.0083 & 0 \\ 0 & 0 & 0.00167 \end{bmatrix}$ kgm^2
Orbital Angular Velocity of LEO at 400 km	0.0011 rad/s^2
Gain Matrix G for $\boldsymbol{q}_{ev}$	$\begin{bmatrix} 20 & 0 & 0 \\ 0 & 20 & 0 \\ 0 & 0 & 20 \end{bmatrix}$
Conventional Sliding Mode Controller Gain — $U_{\max}$	$\begin{bmatrix} 0.01 & 0 & 0 \\ 0 & 0.01 & 0 \\ 0 & 0 & 0.01 \end{bmatrix}$
Gain in Adaptive Controller Design — K	I_3
Disturbance Torque	$\begin{bmatrix} 10^{-4} & 10^{-4} & 10^{-4} \end{bmatrix}^T N.m$

NOTE: In the results provided, it can be noted that the plots labelled '*CSMC*' denote the time responses due to the control action of the Conventional Sliding Mode controller. The

plots labelled 'AC' represent the time responses due to the control action of the Adaptive Controller. The plots labelled '*SMCD*' refer to the responses due to the control influence of the proposed Sliding Mode Control with the Disturbance Estimator.

Case 1: For this case, Table 6.2 provides the details of the initial body-frame quaternion, orbital-frame quaternion and the chosen gain for the proposed Sliding Mode Control strategy, $U_{\max}$. Based on the simulation time and solver details provided in the previous section, the time-histories for the components of the error angular velocity vector, error quaternion vector, control input, sliding equation and the disturbance estimation were found. It can be noted that the time-histories of the sliding equation plots are applicable for the designed Conventional Sliding Mode Controller and the proposed Sliding Mode Controller with a Disturbance Estimator. The disturbance estimation plots are applicable for the Adaptive Controller and the proposed Sliding Mode Controller with a Disturbance Estimator.

Table 6.2 Numerical Simulation Parameters for Case 1

Parameter Name	Value
Initial Orbital-Frame Quaternion	$\begin{bmatrix}1 & 0 & 0 & 0\end{bmatrix}^T$
Initial Body-Frame Angular Velocity	$\begin{bmatrix}0.01 & -0.01 & 0.01\end{bmatrix}^T$
Initial Body-Frame Quaternion	$\begin{bmatrix}0.993 & 0.0551 & 0.0716 & 0.0782\end{bmatrix}^T$
Gain for Proposed Sliding Mode Controller — $U_{\max}$	$\begin{bmatrix}0.005 & 0 & 0\\ 0 & 0.005 & 0\\ 0 & 0 & 0.005\end{bmatrix}$

Figures 6.1, 6.2, and 6.3 show responses of the error angular velocity components. A selected area shown by the black ellipse is magnified for discussion and analysis purposes. Figure 6.1 shows the x-component of the error angular velocity measured in the body-frame. The settling time is quick for all three controllers. Chattering due to the effect of the discontinuous control action of the sliding mode controllers can be noted in the magnified section based on the response comparison to the continuous AC controller. It can be noted that the response due to the influence of the proposed Sliding Mode controller with the Disturbance Estimator

(*SMCD*) has a lower magnitude of chattering when compared to that of the *CSMC* response. The y-component response of the error angular velocity in Figure 6.2 is similar to the ones to the x-component response in Figure 6.1 with main differences being the quicker settling time of the *CSMC* and lower frequency of chattering in the response due to the *SMCD*. The z-component angular velocity responses in Figure 6.3 have the quickest convergence to near-zero values.

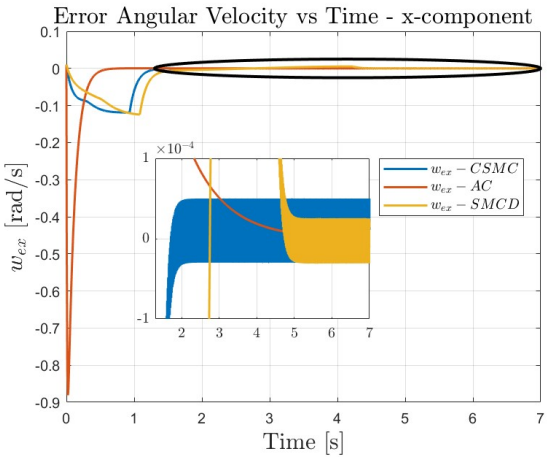

Figure 6.1 Error Angular Velocity Response x - component

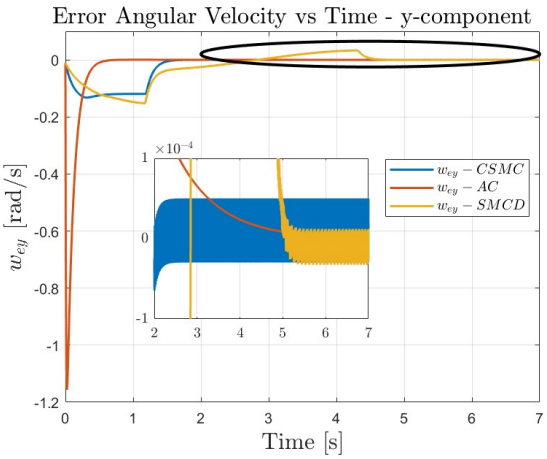

Figure 6.2 Error Angular Velocity Response y - component

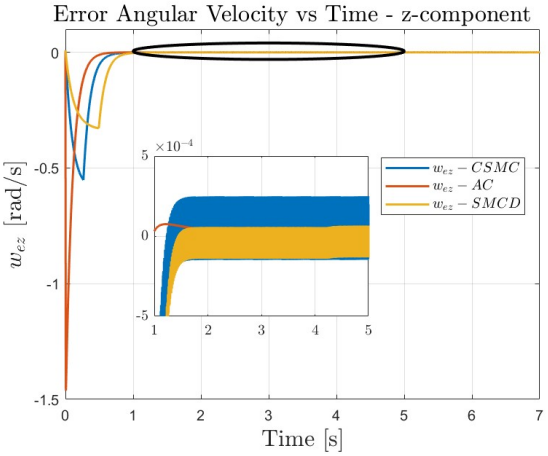

Figure 6.3 Error Angular Velocity Response z - component

In all three components of the error angular velocity, the *SMCD* response shows lower levels

of chattering in comparison to the *CSMC* response as a result of the disturbance estimation and the reduction of the sliding mode control gain, $U_{\max}$. The continuous *AC* structure provides the quickest convergence to zero; however, the transient responses show a comparitively large change in the error angular velocity.

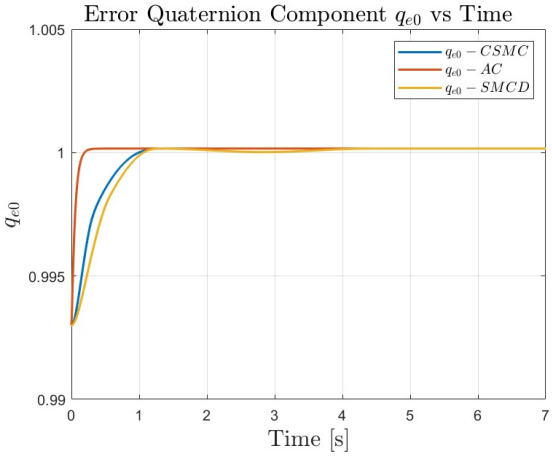

Figure 6.4 Error Quaternion Response - q_{e0}

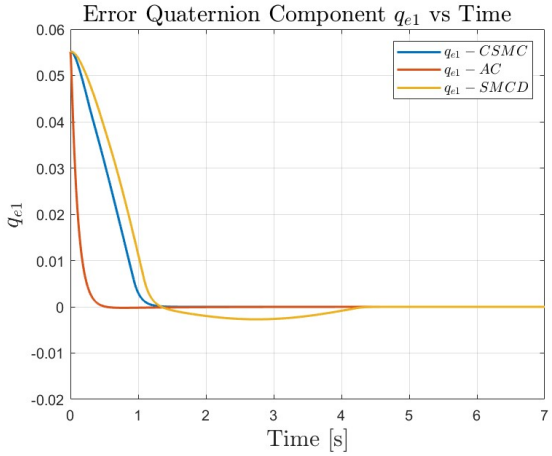

Figure 6.5 Error Quaternion Response - q_{e1}

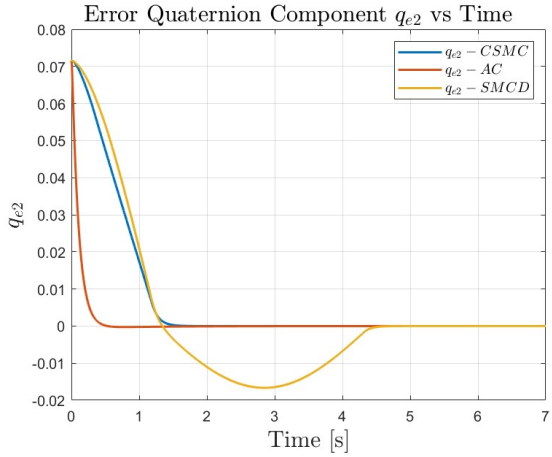

Figure 6.6 Error Quaternion Response - q_{e2}

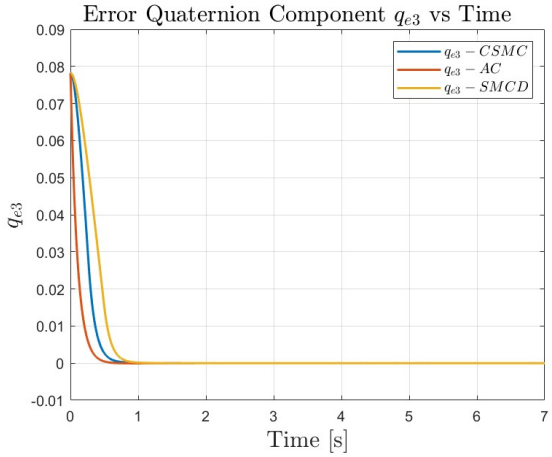

Figure 6.7 Error Quaternion Response - q_{e3}

The error quaternion responses are shown in Figures 6.4 - 6.7. As expected, the scalar component of the quaternion error converges to 1. The fastest convergence, as noted from Figure 6.4, is due to the control action of the *AC*. The *CSMC* action is also quick, taking approximately 1 second. The settling time due to the *SMCD* action is slightly slower than the *CSMC*

action. This trend can also be noted in the responses for the vector components of the error quaternion. Although the levels of chattering in the error angular velocity are reduced with use of the *SMCD*, as noted previously, there is a trade-off for this in the quaternion convergence time to the identity quaternion based on the figures above. The quickest convergence of the vector components of the error quaternion is achieved with the use of the continuous *AC*.

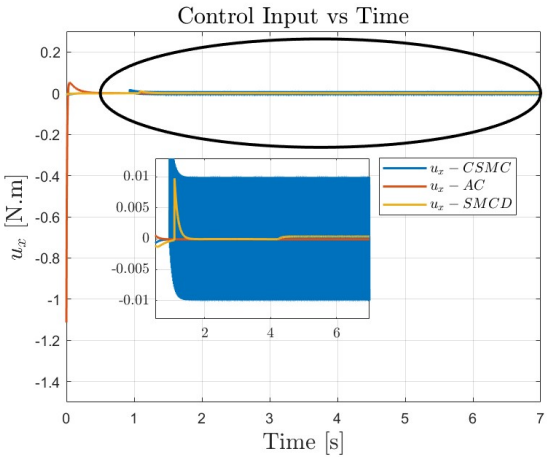

Figure 6.8 Control Input - u_1

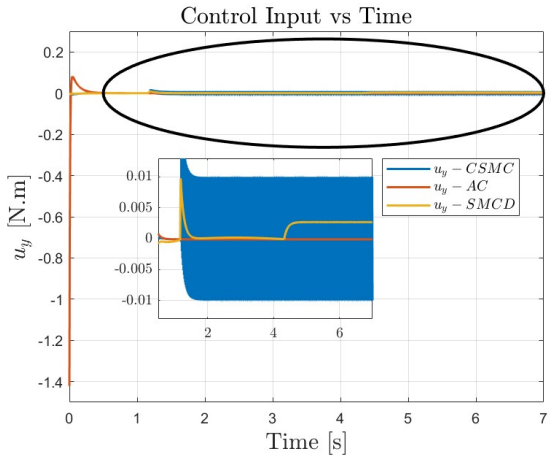

Figure 6.9 Control Input - u_2

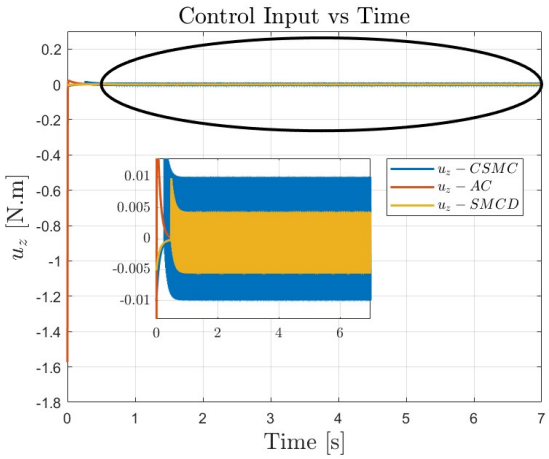

Figure 6.10 Control Input - u_3

The control input plots are shown in Figures 6.8 - 6.10. The continuous nature of the *AC* control action can be seen clearly in Figures 6.8 and 6.9. Chattering due to the discontinuous nature of the sliding mode controllers can also be noted from the magnified sections within

all three control input plots. From the control input plots, it can be reiterated, that due to the disturbance estimation and the reduced sliding mode control gain, $U_{\max}$, the chattering magnitude is reduced when *SMCD* action is employed.

The sliding equation is plotted against time in Figures 6.11 - 6.13. The finite-time convergence to $\boldsymbol{s} = 0$ can be seen in all three plots.

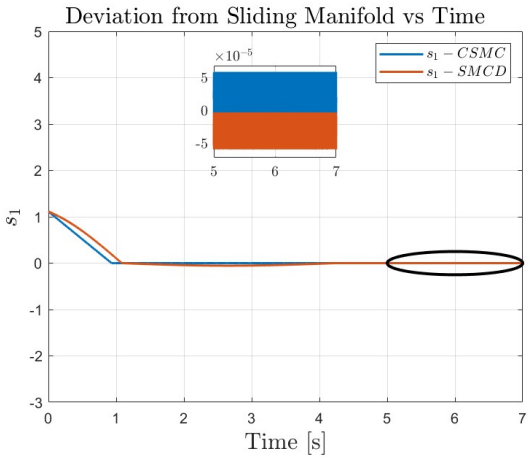

Figure 6.11 Sliding Variable - s_1

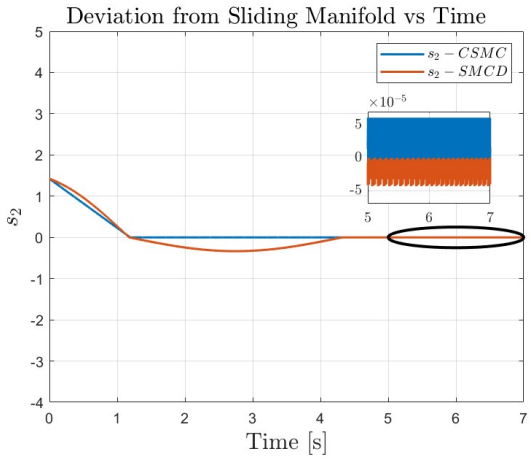

Figure 6.12 Sliding Variable - s_2

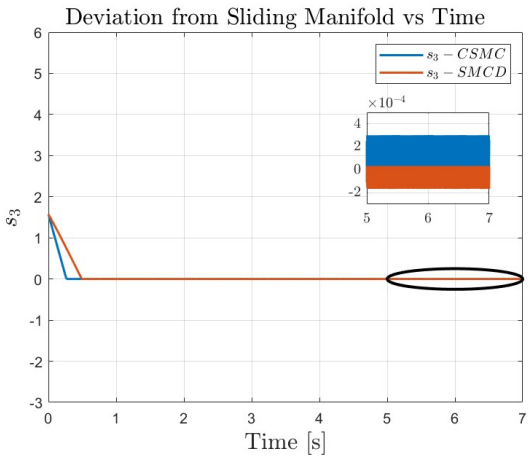

Figure 6.13 Sliding Variable - s_3

As a result of the inclusion of the disturbance bound term while bounding V in Equation 4.41, the reaching time to the sliding manifold will be different than the reaching time

guaranteed by the *CSMC* action. This notion is seen in the sliding equation plots, where the sliding equation takes longer to converge to the sliding manifold when *SMCD* action is employed. As the error angular velocity and the error quaternion states reach $\boldsymbol{s} = 0$, the high-frequency switching nature of the sliding mode control action to ensure to keep the states at the manifold can be seen. Chattering is clearly reduced with the use of the *SMCD* action as noted in the magnified section within all three plots.

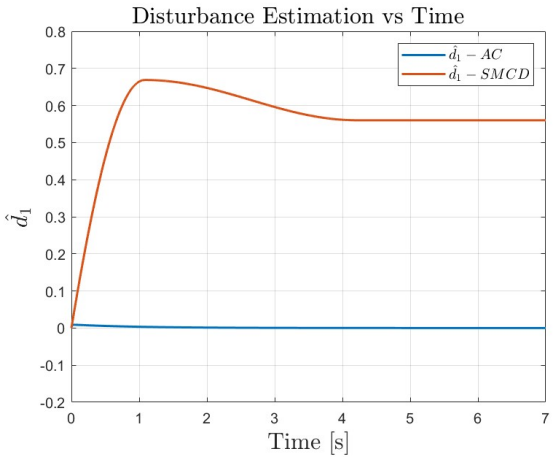

Figure 6.14 Disturbance Estimation - $\hat{d}_1$

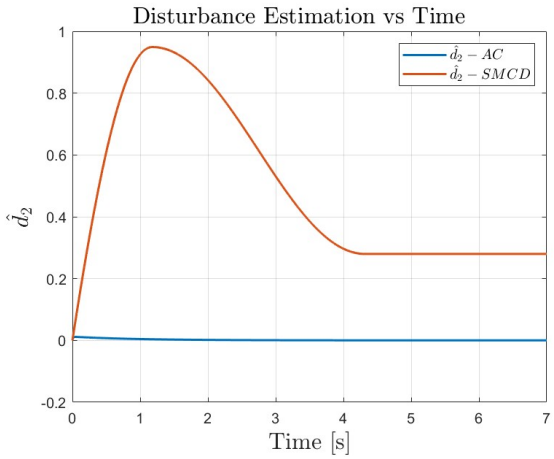

Figure 6.15 Disturbance Estimation - $\hat{d}_2$

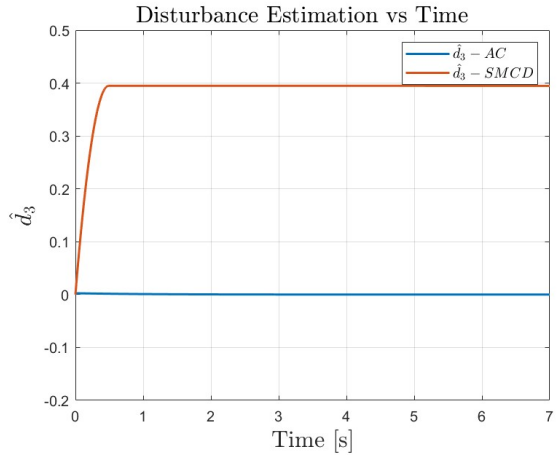

Figure 6.16 Disturbance Estimation - $\hat{d}_3$

Disturbance estimation is performed using the Lyapunov analysis in Equations 4.28 and 4.39. Figures 6.14 - 6.16 show the time-histories of the disturbance estimation for the *AC*

and the SMC controller. The disturbance estimation included in the AC and $SMCD$ control action guarantee convergence to a bounded disturbance estimate. However, the convergence of the disturbance estimation to the true value of the disturbance torque used for simulation purposes will depend on persistence of excitation for both cases and cannot be analyzed from just the figures. The disturbance estimation performed with the use of the $SMCD$ action could be improved if the discontinuous control can be replaced by a smoother, continuous control within a boundary layer around the sliding manifold. However, the Lyapunov analysis may become cumbersome.

Case 2: For this case, a larger misalignment angle is considered and the simulation parameters are detailed in Table 6.3. The results for the components of the error angular velocity, error quaternion, control input, sliding equation and the disturbance estimation were plotted again based on different simulation parameters. The solver and the step-time remained unchanged, however the simulation time was increased to 15 seconds to note the convergence because of the large angle misalignment.

Table 6.3 Numerical Simulation Parameters for Case 2

Parameter Name	Value
Initial Orbital-Frame Quaternion	$\begin{bmatrix} 1 & 0 & 0 & 0 \end{bmatrix}^T$
Initial Body-Frame Angular Velocity	$\begin{bmatrix} 0.01 & -0.01 & 0.01 & 0.0782 \end{bmatrix}^T$
Initial Body-Frame Quaternion	$\begin{bmatrix} 0.918 & 0.188 & 0.225 & 0.266 \end{bmatrix}^T$
Gain for Proposed Sliding Mode Controller — $U_{\max}$	$\begin{bmatrix} 0.005 & 0 & 0 \\ 0 & 0.005 & 0 \\ 0 & 0 & 0.005 \end{bmatrix}$

The response plots for the error angular velocity components for Case 2 are provided in Figures 6.17 - 6.19. There are clear differences between the settling times seen in Case 1 and Case 2. The fastest convergence to zero angular velocity is again provided with the use of the AC action. Although the settling time is larger, the level of chattering seen in the

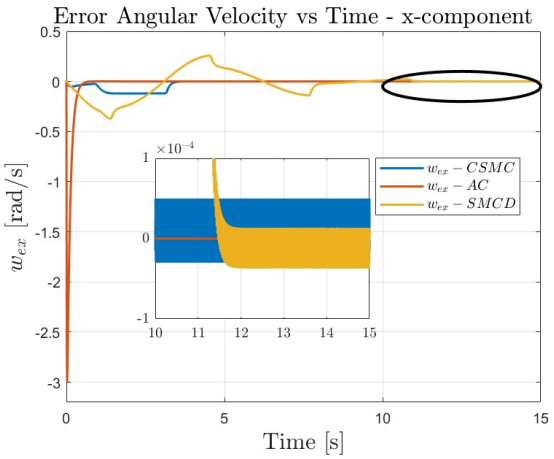

Figure 6.17 Error Angular Velocity Response x - component

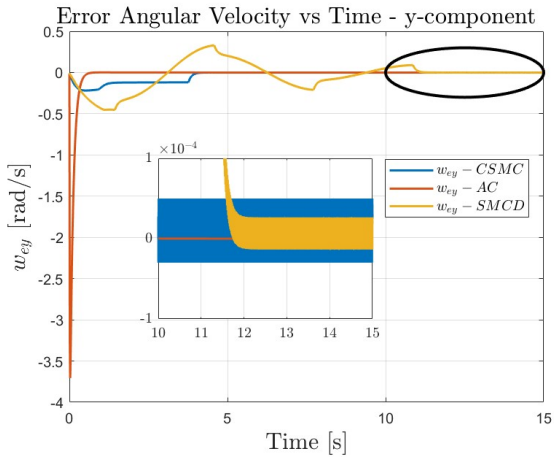

Figure 6.18 Error Angular Velocity Response y - component

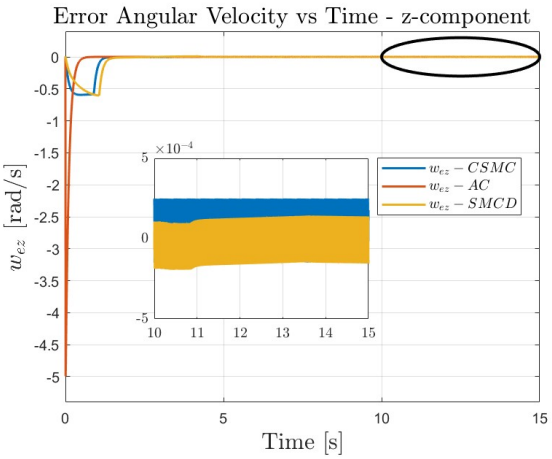

Figure 6.19 Error Angular Velocity Response z - component

error angular velocity components in the magnified section of the plots is lower when the *SMCD* control action is employed as opposed to the *CSMC* action. The transient response times for the x and y components of the error angular velocities are large when *SMCD* is employed. *CSMC* action provides a comparatively faster convergence at the expense of high chattering. Fastest convergence to zero can be noted in the plot for the z-component of the error angular velocity, where the settling time due to the actions of *SMCD* and *CSMC* are similar.

The error quaternion responses are shown in Figures 6.20 - 6.23. The scalar component of the error quaternion converges to 1 as expected. The fastest convergence is obtained with the use of the *AC* action. The *CSMC* control action provides a fast convergence time of below 5 seconds. The *SMCD* control action takes approximately 11 seconds to converge to the identity quaternion and reflects some oscillatory behavior in the time-history of q_{e0}. The time-histories of q_{e1} and q_{e2} are similar, with *SMCD* action taking longer than *AC* and *CSMC* action to provide convergence to zero. q_{e3} is the quickest to converge to zero, and the *CSMC* and *SMCD* actions yield similar settling times. It can again be noted that, although the *SMCD* design reduces chattering, there is a trade-off for it in terms of the convergence time and oscillatory behavior in the error quaternion components in the case of large angle maneuvers.

The control inputs for Case 2 can be noted in the plots in Figures 6.24 - 6.26. The effect of including the disturbance estimation in the equivalent control component and subsequent reduction of the sliding mode gain, $U_{\max}$, can be understood better from Case 2 than Case 1. It can be seen that the *SMCD* input yields less high-frequency switching and as a result, lesser chattering, than that seen in the *CSMC* plots in all three components of the control input once the sliding manifold is reached. The continuous nature of the *AC* controller can be noted in the plots for u_2 and u_3.

The sliding equation is plotted against time in Figures 6.27 - 6.29 to show the finite-time convergence of the error angular velocity and error quaternion states to $\boldsymbol{s} = 0$. In comparison to the results for the sliding equation obtained in Case 1, it can be seen that, for large variations in the initial conditions, the proposed *SMCD* control action takes a longer time to enforce the convergence of the states to $\boldsymbol{s} = 0$ and an oscillatory convergence is induced. However, once the error angular velocity and error quaternion states reach the sliding manifold, chattering is reduced as noted in the magnified sections of the plots.

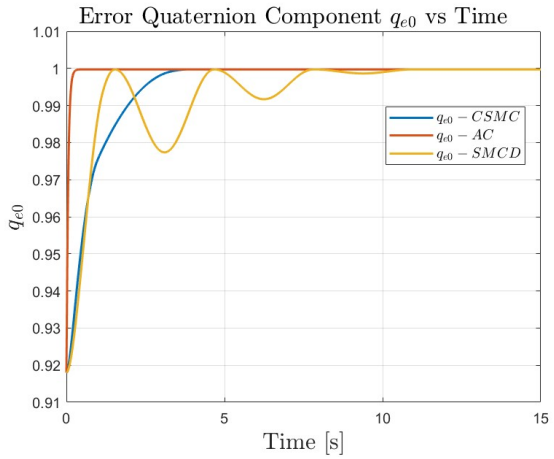

Figure 6.20 Error Quaternion Response - q_{e0}

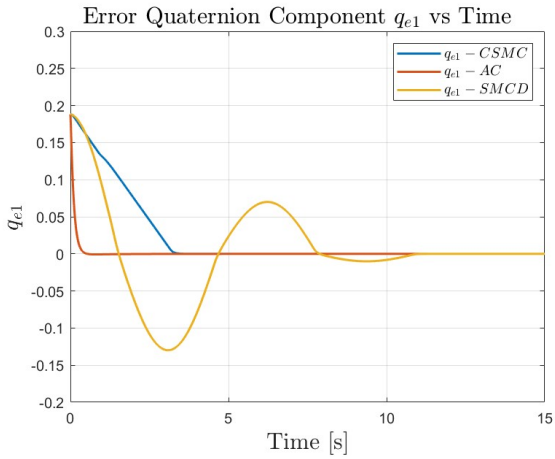

Figure 6.21 Error Quaternion Response - q_{e1}

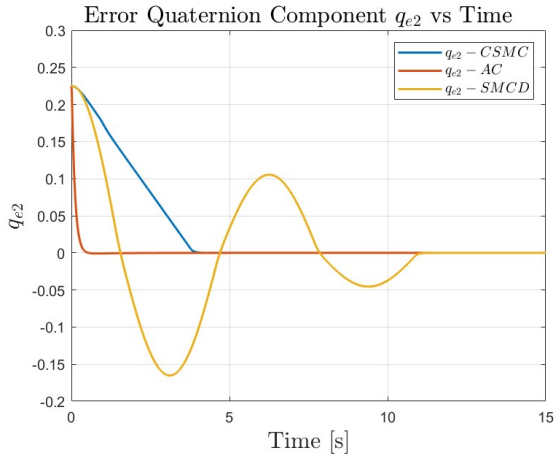

Figure 6.22 Error Quaternion Response - q_{e2}

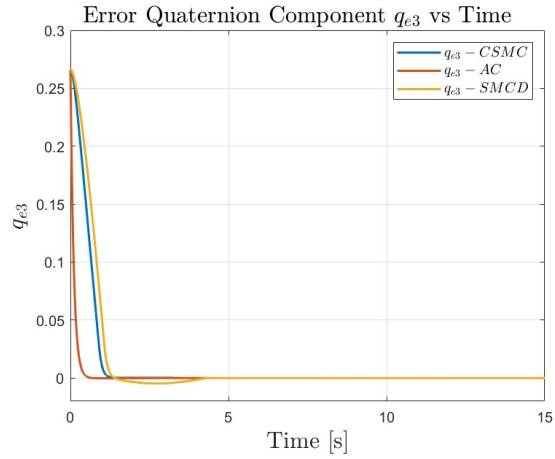

Figure 6.23 Error Quaternion Response - q_{e3}

The disturbance estimation time-histories for Case 2 are provided in Figures 6.30 - 6.32. Similar to the results obtained for Case 1, the disturbance estimation performed using the *AC* and the *SMCD* control action both converge to a bounded disturbance estimate. The convergence to the true value of disturbance torque used for simulation purposes will depend on the persistence of excitation condition. Due to the large variation of the initial conditions, the disturbance estimation via the *SMCD* action was much larger than expected and more inaccurate than that seen in Case 1. Improvements can be made to the disturbance estimation structure to reduce the trade-off between chattering reduction and control perfor-

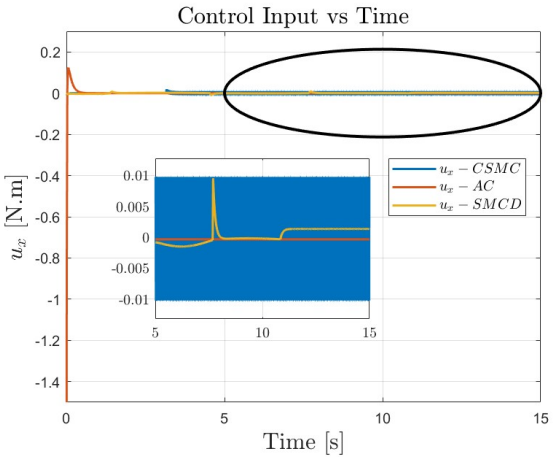

Figure 6.24 Control Input - u_1

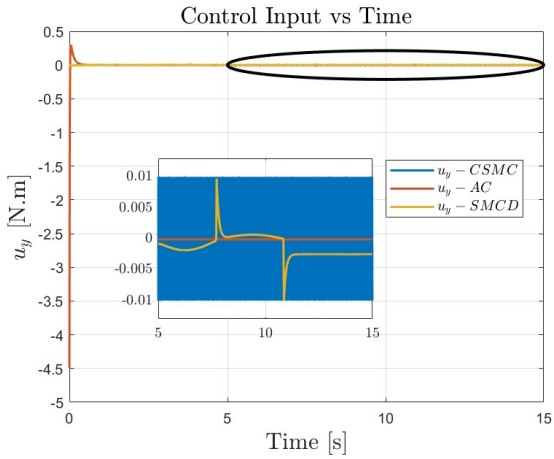

Figure 6.25 Control Input - u_2

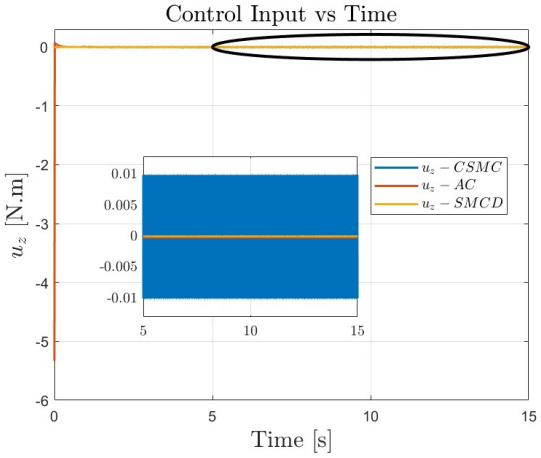

Figure 6.26 Control Input - u_3

mance with consideration that the disturbance estimation is more effective for small angle misalignment between the body-frame and the inertial frame. Furthermore, the disturbance estimations performed can also be studied further by analyzing the persistence of excitation condition and considering a smaller difference between the *AC* gain the the *SMCD* gain.

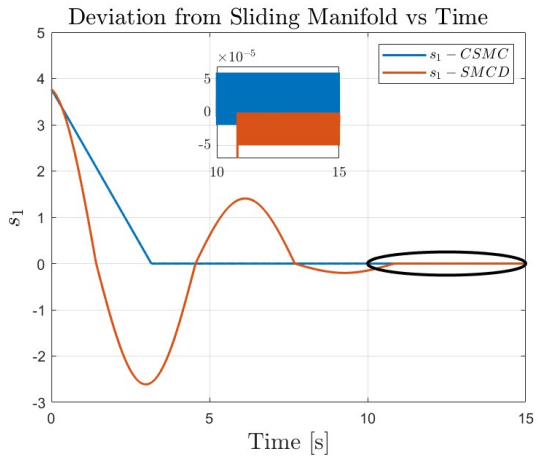

Figure 6.27 Sliding Variable - s_1

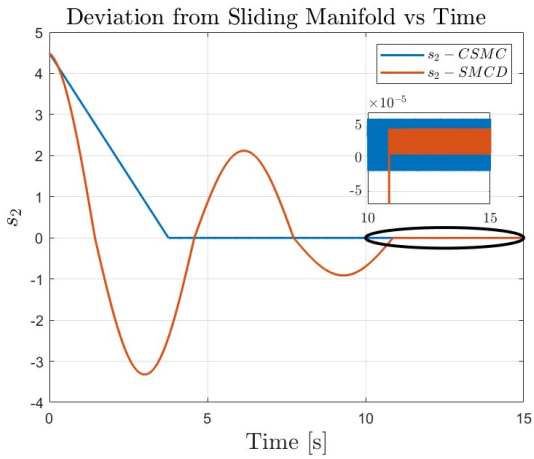

Figure 6.28 Sliding Variable - s_2

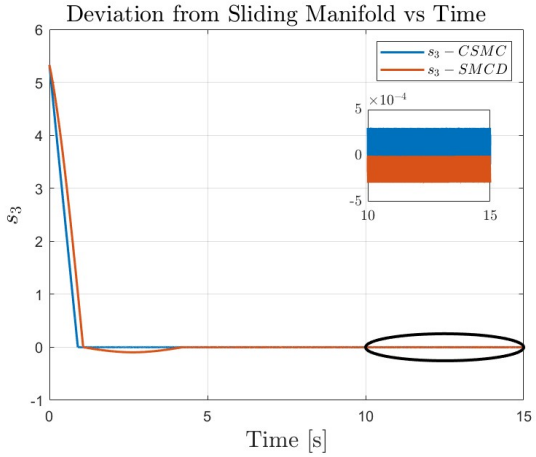

Figure 6.29 Sliding Variable - s_3

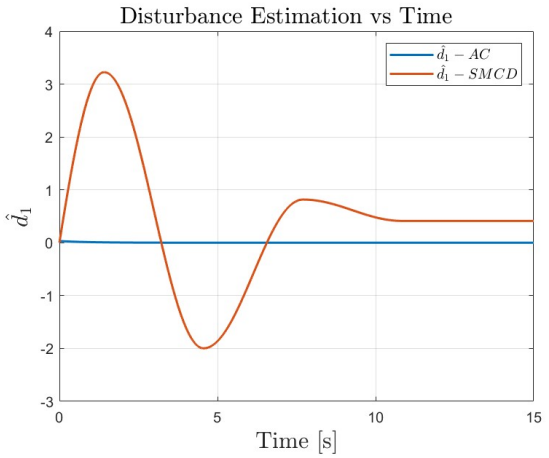

Figure 6.30 Disturbance Estimation - $\hat{d}_1$

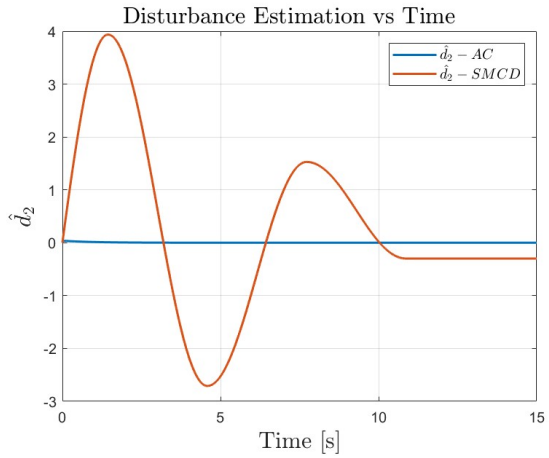

Figure 6.31 Disturbance Estimation - $\hat{d}_2$

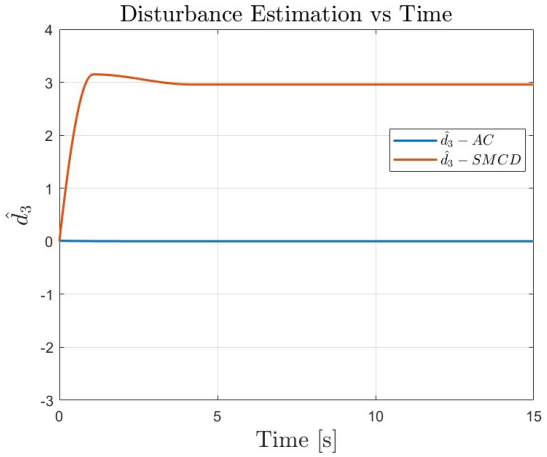

Figure 6.32 Disturbance Estimation - $\hat{d}_3$

7 Conclusions

The spacecraft was first modeled using quaternion kinematics and Euler's rotational equations of motion. The Conventional Sliding Mode Controller, Adaptive Controller and the Proposed Sliding Mode Controller with the Disturbance Estimator were designed using Lyapunov analysis. Simulations were then performed using MATLAB's Simulink environment to obtain results. Based on the kinematics, kinetics and control design, it was inferred that including a disturbance estimation term along with the equivalent control term in Conventional Sliding Mode Control yielded lesser chattering. However, there was a clear trade-off between the control performance and the reduction of chattering. For the cases tested using the proposed control methodology, Adaptive Control and Conventional Sliding Mode Control, the results showed that the continuous Adaptive Controller yielded the fastest convergence to zero error angular velocity and identity error quaternion, which can be owed to the comparatively larger gain used for the Adaptive Controller. To further study which of these methods have a disturbance estimate closer to the true value of the disturbance torque used for simulation purposes, persistence of excitation must be considered. The Conventional Sliding Mode Controller and the Sliding Mode Controller with the Disturbance Estimator ensured convergence to the sliding manifold and a small region around the sliding manifold defined by the disturbance bound respectively, implying convergence to zero error angular velocity and identity error quaternion. For a better comparison of performance between all three control methods, the Sliding Mode Controller gain (U_{max}) and the Adaptive Controller gain (K) should be of similar order of magnitude. Using the proposed Sliding Mode Controller with the Disturbance Estimator, chattering was reduced, however, the convergence time was larger and the disturbance estimate was inaccurate. To improve the results further, changes can be made to the disturbance estimation structure. Another point to note is that the inclusion of equivalent control within the control structure is quite expensive computationally and requires knowledge of all the states. This study assumed that all states are available and the disturbance is constant, which may not be the case during space missions.

Future considerations to refine this study further would involve the use of dual-quaternions for the kinematics, inclusion of bounded uncertainties in the moment of inertia matrix and an attempt to estimate time-varying disturbances while employing Sliding Mode Control with the aim of chattering reduction.

REFERENCES

[1] Utkin, V., "Variable Structure Systems with Sliding Modes," *IEEE Transactions on Automatic Control*, Vol. 22, No. 1, 1977, pp. 212–222. https://doi.org/10.1109/TAC.1977.1101446.

[2] Young, K., Utkin, V., and Ozguner, U., "A control engineer's guide to sliding mode control," *IEEE Transactions on Control Systems Technology*, Vol. 7, No. 3, 2003, pp. 328–342. https://doi.org/10.1109/87.761053.

[3] Utkin, V. I., *Sliding modes and their application in variable structure systems*, Mir Publishers, 1978.

[4] Utkin, V., Poznyak, A., Orlov, Y. V., and Polyakov, A., *Sliding modes and their application in variable structure systems*, SpringerBriefs in Mathematics, Springer International Publishing, 2020.

[5] Nemati, H., Bando, M., and Hokamoto, S., "Chattering Attenuation Sliding Mode Approach for Nonlinear Systems," *Asian journal of control*, Vol. 19, No. 4, 2017, pp. 1519–1531. https://doi.org/10.1002/asjc.1477.

[6] Kachroo, P., and Tomizuka, M., "Chattering reduction and error convergence in the sliding-mode control of a class of nonlinear systems," *IEEE transactions on automatic control*, Vol. 41, No. 7, 1996, pp. 1063–1068. https://doi.org/10.1109/9.508917.

[7] Lee, H., and Utkin, V. I., "Chattering suppression methods in sliding mode control systems," *Annual reviews in control*, Vol. 31, No. 2, 2007, pp. 179–188. https://doi.org/10.1016/j.arcontrol.2007.08.001.

[8] Venkataraman, S. T., and Gulati, S., "Control of Nonlinear Systems Using Terminal Sliding Modes," *Journal of Dynamic Systems, Measurement, and Control*, Vol. 115, No. 3, 1993, pp. 554–560. https://doi.org/10.1115/1.2899138.

[9] Yu, X., Feng, Y., and Man, Z., "Terminal Sliding Mode Control – An Overview," *IEEE Open Journal of the Industrial Electronics Society*, Vol. 2, 2021, pp. 36–52. https://doi.org/10.1109/OJIES.2020.3040412.

[10] Boukattaya, M., and Gassara, H., "Time varying nonsingular terminal sliding mode control for uncertain second order nonlinear systems with prespecified time," *International journal of adaptive control and signal processing*, Vol. 36, No. 8, 2022, pp. 2017–2040. https://doi.org/10.1002/acs.3445.

[11] Su, Y., "Derivative and integral terminal sliding mode control for a class of MIMO nonlinear systems," *Automatica (Oxford)*, Vol. 147, No. 110700-, 2003, pp. 169–175. https://doi.org/10.1016/j.automatica.2022.110700.

[12] Levant, A., "Higher-order sliding modes, differentiation and output-feedback control," *International journal of control*, Vol. 76, No. 9-10, 2003, pp. 924–941. https://doi.org/10.1080/0020717031000099029.

[13] Levant, A., "Homogeneity approach to high-order sliding mode design," *Automatica (Oxford)*, Vol. 41, No. 5, 2005, pp. 823–830. https://doi.org/10.1016/j.automatica.2004.11.029.

[14] Pukdeboon, C., Zinober, A., and Thein, M.-W., "Quasi-continuous higher-order sliding mode controller designs for spacecraft attitude tracking manoeuvres," *2008 International Workshop on Variable Structure Systems*, 2008, pp. 215–220.

[15] Zou, A.-M., Kumar, K. D., Hou, Z.-G., and Liu, X., "Finite-Time Attitude Tracking Control for Spacecraft Using Terminal Sliding Mode and Chebyshev Neural Network," *IEEE transactions on systems, man and cybernetics. Part B, Cybernetics*, Vol. 41, No. 4, 2011, pp. 950–963. https://doi.org/10.1109/TSMCB.2010.2101592.

[16] Yuan, X., Chen, Z., Yuan, Y., and Huang, Y., "Design of fuzzy sliding mode controller for hydraulic turbine regulating system via input state feedback linearization method,"

Energy (Oxford), Vol. 93, 2015, pp. 173–187. https://doi.org/10.1016/j.energy.2015.09.025.

[17] Han, S. H., Tran, M. S., and Tran, D. T., "Adaptive sliding mode control for a robotic manipulator with unknown friction and unknown control direction," *Applied sciences*, Vol. 11, No. 9, 2021, pp. 3919–. https://doi.org/10.1109/87.761053.

[18] Rawashdeh, S. A., "Attitude Analysis of Small Satellites Using Model-Based Simulation," *International journal of aerospace engineering*, Vol. 2019, 2019, pp. 1–11. https://doi.org/10.1155/2019/3020581.

[19] Tianyi, Z., Xuemei, R., and Yao, Z., "A fractional order sliding mode controller design for spacecraft attitude control system," *2015 34th Chinese Control Conference (CCC)*, 2015, pp. 3379–3382.

[20] Bai, Y., Biggs, J. D., Wang, X., and Cui, N., "A singular adaptive attitude control with active disturbance rejection," *European journal of control*, Vol. 35, 2017, pp. 50–56. https://doi.org/10.1016/j.ejcon.2017.01.002.

[21] Chen, Z., and Huang, J., "Attitude Tracking and Disturbance Rejection of Rigid Spacecraft by Adaptive Control," *IEEE transactions on automatic control*, Vol. 54, No. 3, 2009, pp. 600–605. https://doi.org/10.1109/TAC.2008.2008350.

[22] Chai, R., Tsourdos, A., Gao, H., Xia, Y., and Chai, S., "Dual-Loop Tube-Based Robust Model Predictive Attitude Tracking Control for Spacecraft With System Constraints and Additive Disturbances," *IEEE transactions on industrial electronics (1982)*, Vol. 69, No. 4, 2022, pp. 4022–4033. https://doi.org/10.1109/TIE.2021.3076729.

[23] Kristiansen, R., Nicklasson, P., and Gravdahl, J., "Satellite Attitude Control by Quaternion-Based Backstepping," *IEEE transactions on control systems technology*, Vol. 17, No. 3, 2009, pp. 227–232. https://doi.org/10.1109/TCST.2008.924576.

[24] Giuseppi, A., Pietrabissa, A., Cilione, S., and Galvagni, L., "Feedback linearization-based satellite attitude control with a life-support device without communications," *Control engineering practice*, Vol. 90, 2019, pp. 221–230. https://doi.org/10.1016/j.conengprac.2019.06.020.

[25] Chen, Y.-P., and Lo, S.-C., "Sliding-mode controller design for spacecraft attitude tracking maneuvers," *IEEE transactions on aerospace and electronic systems*, 1993, pp. 1328–1333.

[26] Schaub, H., and Junkins, J. L., *Analytical mechanics of space systems*, AIAA education series, American Institute of Aeronautics and Astronautics, Inc., 2018.

[27] Utkin, V. I., *Sliding Modes in Control and Optimization*, Springer, 1992.

[28] Sidi, M. J., *Spacecraft dynamics and control : a practical engineering approach*, Cambridge aerospace series ; 7, Cambridge University Press, 1997.

[29] Yang, Y., *Spacecraft modeling, attitude determination, and control : quaternion-based approach*, CRC Press, 2019.

[30] Curtis, H. D., *Orbital Mechanics for Engineering Students*, Fourth edition., Butterworth-Heinemann, 2021.

[31] Vadali, S. R., "Variable-structure control of spacecraft large-angle maneuvers," *Journal of guidance, control, and dynamics*, 1986, pp. 235–239.

[32] Wu, S. N., Sun, X. Y., Sun, Z. W., and Wu, X. D., "Sliding-mode control for staring-mode spacecraft using a disturbance observer," *Proceedings of the Institution of Mechanical Engineers. Part G, Journal of aerospace engineering*, 2010, pp. 215–224.

[33] Clason, C., *Introduction to functional analysis*, Compact Textbooks in Mathematics, Birkhäuser Cham, 2020.

[34] Bhat, S. P., and Bernstein, D. S., "Finite-Time Stability of Continuous Autonomous Systems," *SIAM journal on control and optimization*, 2000, pp. 751–766.